



Available online at <http://scik.org>

Commun. Math. Biol. Neurosci. 2025, 2025:56

<https://doi.org/10.28919/cmbn/9213>

ISSN: 2052-2541

OPTIMAL CONTROL MODEL FOR THE SPATIAL SPREAD OF COVID-19: AN INTERACTING FLUID FLOW APPROACH

DANIEL UGOCHUKWU NNAJI^{1,*}, PHINEAS ROY KIOGORA², JOSEPH KYALO MUNG'ATU³,
GABRIEL CHINEDU NNAJI⁴

¹Department of Mathematics and Statistics, Pan African University, Institute for Basic Science, Technology and Innovation (PAUSTI), Nairobi, Kenya

²Department of Pure and Applied Mathematics, Jomo Kenyatta University of Agriculture and Technology, Nairobi, Kenya

³Department of Statistics and Actuarial Science, Jomo Kenyatta University of Agriculture and Technology, Nairobi, Kenya

⁴Department of Science Education, University of Nigeria, Nsukka, Enugu, Nigeria

Copyright © 2025 the author(s). This is an open access article distributed under the Creative Commons Attribution License, which permits unrestricted use, distribution, and reproduction in any medium, provided the original work is properly cited.

Abstract. This study develops an optimal control model to analyze the spatial and temporal spread of COVID-19 using an interacting fluid flow approach. Susceptible and infected populations are treated as interacting inviscid fluids governed by Euler's equations, allowing for the spatial dynamics of disease transmission to be captured effectively. Control interventions, specifically vaccination (targeting susceptibility) and medical treatment (enhancing recovery rates), are incorporated as key strategies to mitigate the spread of infection. The model's spatio-temporal dynamics are explored using high-order computational methods, namely the weighted essentially non-oscillatory (WENO) scheme for spatial discretization and the fourth-order Runge-Kutta method for time integration. Numerical simulations demonstrate the effectiveness of the proposed controls, emphasizing that a strategic combination of vaccination and treatment significantly reduces disease prevalence, especially in densely populated regions.

*Corresponding author

E-mail address: daniel.nnaji@unn.edu.ng

Received February 26, 2025

This modeling framework offers valuable insights for policymakers, emphasizing efficient resource allocation and strategic intervention planning to manage COVID-19 or similar infectious diseases effectively.

Keywords: COVID-19; spatial transmission; fluid dynamics model; optimal control.

2020 AMS Subject Classification: 92D30, 76B99, 49J20, 35Q92.

1. INTRODUCTION

Mathematical models play a pivotal role in understanding and predicting the dynamics of infectious diseases such as COVID-19 [1, 2]. We present here a simple SIR model that describes the COVID-19 spread within a short period of time, incorporating vital dynamics through constant birth Λ , natural death (μ) rates, disease recovery (γ) rate and additional infection-associated mortality (φ). As described by [3], the ordinary differential equation (ODE) of a simple COVID-19 model is:

$$(1) \quad \begin{aligned} \frac{dS}{dt} &= \Lambda - \beta SI - \mu S, \\ \frac{dI}{dt} &= \beta SI - (\gamma + \varphi + \mu)I, \\ \frac{dR}{dt} &= \gamma I - \mu R, \end{aligned}$$

with force of infection (βSI), describing the disease transmission dynamics, where β is the transmission rate. The basic reproduction number of equation (1) is simply:

$$(2) \quad R_0 = \frac{\beta \Lambda}{\mu(\gamma + \varphi + \mu)}$$

As we stated earlier, this model is tailored for short-term epidemic scenarios, making it well-suited for analyzing the initial phase of COVID-19 outbreak where vital dynamics and rapid disease progression are prominent factors [4].

While the ODE-based model (1) provides a basic understanding of epidemic dynamics, most existing models offer little or no insight into the spatial dynamics of infectious disease spread. As a result, there is a need for models that can better describe when, where, and how an epidemic spreads. To this account, researchers [5, 6, 7] began to propose epidemic models that integrates both space and time parameters, offering better accuracy in predicting localized outbreaks and capturing the diffusion of infections across a heterogeneous landscape.

Inspired by previous applications of (inviscid) fluid dynamics in modeling traffic flows, Cheng and Wang [8] contributed to the study of COVID-19 spatial epidemic spread by proposing a two-phase system that treats the susceptible and infected populations as fluids with movement patterns, while modeling COVID-19 disease transmission as fluid motion. It is worth noting that both susceptible and infected populations are modeled as interacting fluids mirroring the spread of COVID-19 across a spatial domain.

In this work, we contribute to the existing study by improving the work of *Cheng and Wang* and presenting an optimal control model for the spatial spread of COVID-19, using a framework that explores two primary control measures: (i) reducing susceptibility through vaccination and (ii) enhancing recovery rates through effective treatment of the infected individuals. These controls target different phases of the epidemic progression, aiming to curb the spread of COVID-19 by decreasing the number of susceptible individuals and boosting recovery among infected individuals, respectively.

Our approach utilizes a spatial model based on the classic SIR compartment framework [9, 10]. Here, populations over a given location of study interest are referred to as population densities, while both susceptible and infected population densities are treated as inviscid fluids, characterized by Euler's equation to represent the velocity and direction of epidemic spread [11].

The spatio-temporal dynamics of our model are represented by a set of partial differential equations (PDEs) that describes the evolution of the epidemic over space and time. At the onset of the outbreak, the susceptible population typically occupies a vast spatial domain, while infected populations are initially concentrated in specific hotspots of infection. As infected and susceptible individuals come into contact, infection spreads, with susceptible individuals converting into infected ones. This conversion process is central to the two-phase fluid model, where susceptible "fluid" transforms into infected "fluid," continuously altering the densities and spatial distribution of both populations throughout the epidemic [12].

Given the complex pattern of COVID-19 transmission, we assume a macroscopic approach to the spread. Here, the macroscopic assumption treats the susceptible and infected populations as continuous fluids rather than tracking individual movements and behaviors. By modeling these populations as inviscid fluids, our study captures the large-scale dynamics of COVID-19 spread

while ignoring individual-level variability. This approach provides us with the opportunity to use fluid dynamics equations, such as the Euler equations, to describe the motion of these "fluids" and their interaction over space and time. To achieve high-resolution spatial dynamics in our simulations, we employ the high-order weighted essentially non-oscillatory (WENO) scheme, a computational method from fluid dynamics known for its precision in resolving complex, non-linear flow characteristics [13, 14]. Through this advanced computational approach, our model provides valuable insights into the spatio-temporal progression of COVID-19, offering tools for understanding and controlling epidemic spread in different spatial settings.

The remainder of this work is structured as follows: Section 2 presents the formulation of the spatial model, detailing the governing equations and assumptions underlying the fluid dynamics analogy. Section 3 conducts a thorough analysis of the model, including stability assessments and the derivation of key mathematical properties, while Section 4 highlights the spatial and temporal numerical discretization using the WENO-5 and RK4 schemes, respectively. Section 5 introduces the optimal control strategies, outlining the implementation of vaccination and treatment interventions to mitigate disease spread. Section 6 discusses the numerical simulations, illustrating the model's effectiveness through computational experiments. Finally, Section 7 provides conclusions while restating the valuable contributions made.

2. FORMULATION OF THE SPATIAL MODEL

The COVID-19 spatial model is formulated based on the principles of conservation laws in fluid dynamics [9]. To simplify and capture the complexities of its spatial behavior, several core assumptions are introduced: both susceptible and infected populations are treated as continuous densities across the study area. Interactions between these groups are modeled as if they were inviscid, emphasizing a broad-scale perspective of how the disease spreads. The spatial environment is assumed to be uniform, meaning its properties remain constant throughout the domain. At the boundaries, no population movement occurs, reflecting zero-flow boundary conditions. Furthermore, the model likens the behavior of these population groups to an equation of state (the Ideal Gas Law), with temperature kept constant throughout the outbreak. Together, these assumptions form a straightforward yet effective framework for analyzing how the epidemic spreads over time and space [15].

The changes in the densities of the susceptible and infected/infectious populations are modeled using the continuity equation: $\frac{\partial \rho}{\partial t} + \nabla \cdot (\rho V) = \sigma$, which ensures that population densities remain consistent over time [16]. The spread of COVID-19 as a result of the movement of these populations is determined by Euler's equation of motion: $\frac{\partial V}{\partial t} + V \cdot \nabla V = -\frac{1}{\rho} \nabla P$, providing a framework for understanding their velocity profiles.

The two dimensional spatial form of system (1) is therefore:

$$(3) \quad \begin{aligned} \frac{\partial S(t, X)}{\partial t} + \nabla \cdot (S q_s) &= \Lambda - \beta S(t, X) I(t, X) - \mu S(t, X) \\ \frac{\partial I(t, X)}{\partial t} + \nabla \cdot (I q_i) &= \beta S(t, X) I(t, X) - (\gamma + \varphi + \mu) I(t, X) \\ \frac{\partial R(t, X)}{\partial t} &= \gamma I(t, X) - \mu R(t, X) \end{aligned}$$

Where $X = (x, y)$, $\nabla = \frac{\partial}{\partial x} + \frac{\partial}{\partial y}$, $S(t, X)$ is the susceptible population density, $I(t, X)$ is the infected/infectious population density, and $R(t, X)$ is the recovered population density. The parameters $\lambda, \beta, \gamma, \varphi, \mu$ are as defined above in (1). The velocity fields q_s and q_i of the susceptible and infected/infectious compartments are described by Euler's equations and are given by:

$$(4) \quad \begin{aligned} S \frac{\partial q_s}{\partial t} + S q_s \cdot \nabla q_s &= -\nabla P_s, \\ I \frac{\partial q_i}{\partial t} + I q_i \cdot \nabla q_i &= -\nabla P_i, \end{aligned}$$

Where $q_s = (u_s, v_s)$ and $q_i = (u_i, v_i)$. Applying the equation of state which characterizes the fluid pressure P in terms of density, we have from equation (4) that $P_s = k_s S$ and $P_i = k_i I$, where k_s, k_i are constants. This straightforward analogy suggests that the movement of the fluid is influenced by variations in its density gradient. Equations (3) and (4) are subject to the initial and boundary conditions:

$$(5) \quad \begin{cases} S(0, X) > 0, I(0, X) \geq 0, R(0, X) \geq 0 \text{ and } q_s(0, X) = 0, q_i(0, X) = 0 \\ \left. \frac{\partial S}{\partial n} \right|_{\text{boundary}} = 0, \left. \frac{\partial I}{\partial n} \right|_{\text{boundary}} = 0, \left. \frac{\partial R}{\partial n} \right|_{\text{boundary}} = 0, q_s|_{\text{boundary}} = 0, q_i|_{\text{boundary}} = 0 \end{cases}$$

Note: The recovered class will be neglected in the model analysis because the study focuses on the early phase of the COVID-19, where infection spread is the dominant concern.

3. MODEL ANALYSIS

This section conducts the spatial analysis of equation (3) and (4). To proceed, we consider the compartments with spatial terms, together with their velocity fields i.e.:

$$(6) \quad \begin{cases} \frac{\partial S(t,X)}{\partial t} + \nabla \cdot (Sq_s) = \Lambda - \beta S(t,X)I(t,X) - \mu S(t,X) \\ \frac{\partial I(t,X)}{\partial t} + \nabla \cdot (Iq_i) = \beta S(t,X)I(t,X) - (\gamma + \varphi + \mu)I(t,X) \\ S \frac{\partial q_s}{\partial t} + Sq_s \cdot \nabla q_s = -k_s \nabla S, \\ I \frac{\partial q_i}{\partial t} + Iq_i \cdot \nabla q_i = -k_i \nabla I \end{cases}$$

Let us refer to equation (6) as having two cases: Upper-case and Lower-case. Then, multiplying the velocity vectors (q_s, q_i) on both sides of the Upper-case of (6), and adding the results to the corresponding Lower-case of (6), we obtain:

$$(7) \quad \begin{cases} \frac{\partial}{\partial t} (Sq_s) + \nabla \cdot (Sq_s q_s) = -k_s \nabla S + \Lambda q_s - \beta SI q_s - \mu S q_s \\ \frac{\partial}{\partial t} (Iq_i) + \nabla \cdot (Iq_i q_i) = -k_i \nabla I + \beta SI q_i - (\gamma + \varphi + \mu) I q_i \end{cases}$$

Expressing the Upper-case of equation (6), and (7) in their respective x - and y -direction, we obtain:

$$(8) \quad \begin{cases} \frac{\partial S}{\partial t} + \frac{\partial(Su_s)}{\partial x} + \frac{\partial(Sv_s)}{\partial y} = \Lambda - \beta SI - \mu S \\ \frac{\partial(Su_s)}{\partial t} + \frac{\partial(Su_s^2)}{\partial x} + \frac{\partial(Su_s v_s)}{\partial y} = -k_s \frac{\partial S}{\partial x} + \Lambda u_s - \beta SI u_s - \mu S u_s \\ \frac{\partial(Sv_s)}{\partial t} + \frac{\partial(Su_s v_s)}{\partial x} + \frac{\partial(Sv_s^2)}{\partial y} = -k_s \frac{\partial S}{\partial y} + \Lambda v_s - \beta SI v_s - \mu S v_s \\ \frac{\partial I}{\partial t} + \frac{\partial(Iu_i)}{\partial x} + \frac{\partial(Iv_i)}{\partial y} = \beta SI - (\gamma + \varphi + \mu) I \\ \frac{\partial(Iu_i)}{\partial t} + \frac{\partial(Iu_i^2)}{\partial x} + \frac{\partial(Iu_i v_i)}{\partial y} = -k_i \frac{\partial I}{\partial x} + \beta SI u_i - (\gamma + \varphi + \mu) I u_i \\ \frac{\partial(Iv_i)}{\partial t} + \frac{\partial(Iu_i v_i)}{\partial x} + \frac{\partial(Iv_i^2)}{\partial y} = -k_i \frac{\partial I}{\partial y} + \beta SI v_i - (\gamma + \varphi + \mu) I v_i \end{cases}$$

In its compact form, system (8) can be written as:

$$(9a) \quad \frac{\partial U}{\partial t} + \frac{\partial M(U)}{\partial x} + \frac{\partial N(U)}{\partial y} = Q(U)$$

In its explicit form, equation (9a) becomes

$$(9b) \quad \frac{\partial U}{\partial t} + \frac{\partial M}{\partial U} \cdot \frac{\partial U}{\partial x} + \frac{\partial N}{\partial U} \cdot \frac{\partial U}{\partial y} = Q(U)$$

Where

$$U = \begin{pmatrix} S \\ Su_s \\ Sv_s \\ I \\ Iu_i \\ Iv_i \end{pmatrix}, M(U) = \begin{pmatrix} Su_s \\ Su_s^2 + k_s S \\ Su_s v_s \\ Iu_i \\ Iu_i^2 + k_i I \\ Iu_i v_i \end{pmatrix}, M(U) = \begin{pmatrix} Sv_s \\ Su_s v_s \\ Sv_s^2 + k_s S \\ Iv_i \\ Iu_i v_i \\ Iv_i^2 + k_i I \end{pmatrix}, Q(U) = \begin{pmatrix} \Lambda - \beta SI - \mu S \\ \Lambda u_s - \beta SIu_s - \mu Su_s \\ \Lambda v_s - \beta SIv_s - \mu Sv_s \\ \beta SI - (\gamma + \varphi + \mu)I \\ \beta SIu_i - (\gamma + \varphi + \mu)Iu_i \\ \beta SIv_i - (\gamma + \varphi + \mu)Iv_i \end{pmatrix}.$$

We note that $\frac{\partial M}{\partial U}$ and $\frac{\partial N}{\partial U}$ are referred to as the Jacobian of F and G respectively. Thus, the Jacobian matrices now becomes

$$(10) \quad J_M = \frac{\partial M}{\partial U} = \begin{pmatrix} 0 & 1 & 0 & 0 & 0 & 0 \\ k_s - u_s^2 & 2u_s & 0 & 0 & 0 & 0 \\ -u_s v_s & v_s & u_s & 0 & 0 & 0 \\ 0 & 0 & 0 & 0 & 1 & 0 \\ 0 & 0 & 0 & k_i - u_i^2 & 2u_i & 0 \\ 0 & 0 & 0 & -u_i v_i & v_i & u_i \end{pmatrix}$$

and

$$(11) \quad J_N = \frac{\partial N}{\partial U} = \begin{pmatrix} 0 & 0 & 1 & 0 & 0 & 0 \\ -u_s v_s & v_s & u_s & 0 & 0 & 0 \\ k_s - v_s^2 & 0 & 2v_s & 0 & 0 & 0 \\ 0 & 0 & 0 & 0 & 0 & 1 \\ 0 & 0 & 0 & -u_i v_i & v_i & u_i \\ 0 & 0 & 0 & k_i - v_i^2 & 0 & 2v_i \end{pmatrix}$$

It is clear to see that for any two numbers $m, n \in \mathbb{R}$, the resulting matrix

$$(12) \quad m \frac{\partial M}{\partial U} + n \frac{\partial N}{\partial U} = \begin{pmatrix} 0 & m & n & 0 & 0 & 0 \\ m(k_s - u_s^2) - nu_s v_s & 2mu_s + nv_s & nu_s & 0 & 0 & 0 \\ -mu_s v_s + n(k_s - v_s^2) & mv_s & mu_s + 2nv_s & 0 & 0 & 0 \\ 0 & 0 & 0 & 0 & m & n \\ 0 & 0 & 0 & m(k_i - u_i^2) - nu_i v_i & 2mu_i + nv_i & nu_i \\ 0 & 0 & 0 & -mu_i v_i + n(k_i - v_i^2) & mv_i & mu_i + 2nv_i \end{pmatrix}$$

has the eigenvalues:

$$\begin{aligned}\lambda_1 &= mu_s + nv_s, & \lambda_{2,3} &= mu_s + nv_s \pm \sqrt{k_s(m^2 + n^2)} \\ \lambda_4 &= mu_i + nv_i, & \lambda_{5,6} &= mu_i + nv_i \pm \sqrt{k_i(m^2 + n^2)}.\end{aligned}$$

Then, it suffices to say that by [13],[8] and [12], system (9a) is hyperbolic.

Analyzing system (9a) can often be challenging, so a linear approach is chosen instead. To linearize the hyperbolic PDE (9a), we assume U is perturbed around a steady state U_0 , such that $U = U_0 + \delta U$, where δU represents a small perturbation. At steady state,

$$(13) \quad U_0 = [S_0 \ S_0 u_s^0 \ S_0 v_s^0 \ I_0 \ I_0 u_i^0 \ I_0 v_i^0]^T = \left[\frac{\Lambda}{\mu} \ 0 \ 0 \ 0 \ 0 \ 0 \right]^T$$

But the steady state (13) is likened to the disease-free-equilibrium of the system. To proceed with the linear analysis, we expand $M(U)$ and $N(U)$ about U_0 using Taylor series neglecting higher order terms ($\delta U^2, \delta U^3, \dots$):

$$(14) \quad M(U) \approx M(U_0) + \left. \frac{\partial M}{\partial U} \right|_{U_0} \cdot \delta U_0, \text{ and } N(U) \approx N(U_0) + \left. \frac{\partial N}{\partial U} \right|_{U_0} \cdot \delta U_0$$

Substituting $U = U_0 + \delta U$ into system (9a) leads to:

$$(15) \quad \frac{\partial(U_0 + \delta U)}{\delta t} + \left. \frac{\partial M}{\partial U} \right|_{U_0} \cdot \frac{\partial(U_0 + \delta U)}{\delta x} + \left. \frac{\partial N}{\partial U} \right|_{U_0} \cdot \frac{\partial(U_0 + \delta U)}{\delta y} = Q(U_0) + \left. \frac{\partial Q}{\partial U} \right|_{U_0} \cdot \delta U$$

Simplifying equation (15), noting that U_0 satisfies the steady-state equation and $Q(U_0)$ is a zero matrix, we have that the linearized equation becomes:

$$(16) \quad \frac{\partial(\delta U)}{\delta t} + \left. \frac{\partial M}{\partial U} \right|_{U_0} \cdot \frac{\partial(\delta U)}{\delta x} + \left. \frac{\partial N}{\partial U} \right|_{U_0} \cdot \frac{\partial(\delta U)}{\delta y} = \left. \frac{\partial Q}{\partial U} \right|_{U_0} \cdot \delta U$$

Then, making a variable transformation $\delta U \rightarrow \widehat{U}$, we have that equation (16) becomes

$$(17) \quad \frac{\partial \widehat{U}}{\delta t} + \left. \frac{\partial M}{\partial U} \right|_{U_0} \cdot \frac{\partial \widehat{U}}{\delta x} + \left. \frac{\partial N}{\partial U} \right|_{U_0} \cdot \frac{\partial \widehat{U}}{\delta y} = \left. \frac{\partial Q}{\partial U} \right|_{U_0} \cdot \widehat{U}$$

Where

$$(18) \quad \left. \frac{\partial M}{\partial U} \right|_{U_0} = \begin{pmatrix} 0 & 1 & 0 & 0 & 0 & 0 \\ k_s & 0 & 0 & 0 & 0 & 0 \\ 0 & 0 & 0 & 0 & 0 & 0 \\ 0 & 0 & 0 & 0 & 1 & 0 \\ 0 & 0 & 0 & k_i & 0 & 0 \\ 0 & 0 & 0 & 0 & 0 & 0 \end{pmatrix}, \quad \left. \frac{\partial N}{\partial U} \right|_{U_0} = \begin{bmatrix} 0 & 0 & 1 & 0 & 0 & 0 \\ 0 & 0 & 0 & 0 & 0 & 0 \\ k_s & 0 & 0 & 0 & 0 & 0 \\ 0 & 0 & 0 & 0 & 0 & 1 \\ 0 & 0 & 0 & 0 & 0 & 0 \\ 0 & 0 & 0 & k_i & 0 & 0 \end{bmatrix}$$

and

$$(19) \quad \frac{\partial Q}{\partial U} = \begin{pmatrix} -\beta I - \mu & 0 & 0 & -\beta S & 0 & 0 \\ -\frac{\Lambda u_s}{S} & \frac{\Lambda}{S} - \beta I - \mu & 0 & -\beta S u_s & 0 & 0 \\ -\frac{\Lambda v_s}{S} & 0 & \frac{\Lambda}{S} - \beta I - \mu & -\beta S v_s & 0 & 0 \\ \beta I & 0 & 0 & \beta S - (\gamma + \mu + \varphi) & 0 & 0 \\ \beta I u_i & 0 & 0 & 0 & \beta S - (\gamma + \mu + \varphi) & 0 \\ \beta I v_i & 0 & 0 & 0 & 0 & \beta S - (\gamma + \mu + \varphi) \end{pmatrix}$$

At steady state

$$(20) \quad \left. \frac{\partial Q}{\partial U} \right|_{U_0} = \begin{pmatrix} -\mu & 0 & 0 & -\frac{\Lambda \beta}{\mu} & 0 & 0 \\ 0 & 0 & 0 & 0 & 0 & 0 \\ 0 & 0 & 0 & 0 & 0 & 0 \\ 0 & 0 & 0 & \frac{\Lambda \beta}{\mu} - (\gamma + \mu + \varphi) & 0 & 0 \\ 0 & 0 & 0 & 0 & \frac{\Lambda \beta}{\mu} - (\gamma + \mu + \varphi) & 0 \\ 0 & 0 & 0 & 0 & 0 & \frac{\Lambda \beta}{\mu} - (\gamma + \mu + \varphi) \end{pmatrix}.$$

We introduce an initial guess

$$(21) \quad \widehat{U} = \bar{U} e^{\eta t} e^{\iota(ax+by+\phi)}$$

where ι defines the imaginary unit which satisfies $\iota^2 = -1$, with a and b representing the wave numbers corresponding to vertical and horizontal distribution of COVID-19 in the location of interest respectively, while ϕ represents the phase shift. Differentiating (21) and substituting the results into (17), we have that since $e^{\eta t} e^{\iota(ax+by+\phi)} \neq 0$, then

$$(22) \quad \left[\eta \mathbb{I} - \left(\left. \frac{\partial Q}{\partial U} \right|_{U_0} - \iota a \left. \frac{\partial M}{\partial U} \right|_{U_0} - \iota b \left. \frac{\partial N}{\partial U} \right|_{U_0} \right) \right] \bar{U} = 0$$

Where \mathbb{I} represents the identity matrix. For a nontrivial solution of \bar{U} , the term η must be an eigenvalue of the resulting matrix: $Z^* = \left. \frac{\partial Q}{\partial U} \right|_{U_0} - \iota a \left. \frac{\partial M}{\partial U} \right|_{U_0} - \iota b \left. \frac{\partial N}{\partial U} \right|_{U_0}$. Therefore, from equation (18) and (20), Z^* becomes:

$$(23) \quad Z^* = \begin{pmatrix} -\mu & -ia & -ib & -\frac{\Lambda\beta}{\mu} & 0 & 0 \\ -iak_s & 0 & 0 & 0 & 0 & 0 \\ -ibk_s & 0 & 0 & 0 & 0 & 0 \\ 0 & 0 & 0 & \frac{\Lambda\beta}{\mu} - (\gamma + \mu + \phi) & -ia & -ib \\ 0 & 0 & 0 & -iak_i & \frac{\Lambda\beta}{\mu} - (\gamma + \mu + \phi) & 0 \\ 0 & 0 & 0 & -ibk_i & 0 & \frac{\Lambda\beta}{\mu} - (\gamma + \mu + \phi) \end{pmatrix}$$

The eigenvalues of matrix (23) are

$$\begin{aligned} \eta_1 &= 0 & \eta_{2,3} &= -\frac{\mu}{2} \pm i \sqrt{k_s(a^2 + b^2) + \frac{\mu^2}{4}} \\ \eta_4 &= \frac{\Lambda\beta}{\mu} - (\gamma + \phi + \mu) & \eta_{5,6} &= \frac{\Lambda\beta}{\mu} - (\gamma + \phi + \mu) \pm i \sqrt{(a^2 + b^2)k_i} \end{aligned}$$

Then, it suffices to say that the first three eigenvalues (η_1, η_2, η_3) describe the wavefront of the susceptible fluid. Since η_2 and η_3 have negative real parts, the zero eigenvalue indicates that the system is at a critical turning point, where even small changes in parameters could lead to significant shifts in disease behavior, such as transitioning from eradication to an outbreak or vice versa. At this point, the system exhibits neutral behavior near the equilibrium point in the direction of the susceptible fluid. This condition is known as marginal stability, which suggests that while the system will neither move away from equilibrium nor return to it if disturbed along this direction, it will remain in a balanced state.

On the other hand, observe that from eigenvalues (η_4, η_5 and η_6), the term $\frac{\Lambda\beta}{\mu} - (\gamma + \phi + \mu) = (R_0 - 1)(\gamma + \phi + \mu)$. It therefore makes sense to say that the last three eigenvalues describes the wave-front of the infected fluid, with a bi-directional propagation speed of $\sqrt{k_i}$ towards the direction determined by the unit vector: $\left(\frac{a}{\sqrt{a^2+b^2}}, \frac{b}{\sqrt{a^2+b^2}} \right)$.

Drawing conclusion from equation (2), if $R_0 < 1$, then, the eigenvalues η_4, η_5, η_6 will have negative real-parts, and as a result, the system will be linearly stable around the equilibrium point U_0 . Otherwise, the system is unstable.

4. THE WENO SCHEME

Here, we propose to spatially discretize the flux terms of the given hyperbolic PDE (9a) using the fifth-order Weighted Essentially Non-Oscillatory (WENO) scheme, and the fourth-order Runge-Kutta (RK4) time-stepping scheme for the temporal discretization.

To proceed, we divide the spatial domain into a uniform grid. In x -direction, the cells are indexed by j and defined as $\mathcal{N}_j = [x_{j-\frac{1}{2}}, x_{j+\frac{1}{2}}]$, while in y -direction, the cells are indexed k and defined as $\mathcal{N}_k = [y_{k-\frac{1}{2}}, y_{k+\frac{1}{2}}]$, where $j = 1, 2, \dots, \mathcal{N}_x$ and $k = 1, 2, \dots, \mathcal{N}_y$. The cell centers are located at (x_j, y_k) , with $x_j = \frac{x_{j+\frac{1}{2}} + x_{j-\frac{1}{2}}}{2}$ and $y_k = \frac{y_{k+\frac{1}{2}} + y_{k-\frac{1}{2}}}{2}$. The flux values at these points are denoted by $M_j = M(x_j)$ and $N_k = N(y_k)$, respectively.

Next we approximate the flux derivatives $\frac{\partial M(U)}{\partial x}$ and $\frac{\partial N(U)}{\partial y}$ at cell center by: $\frac{1}{\Delta x} (\widehat{M}_{j+\frac{1}{2}} - \widehat{M}_{j-\frac{1}{2}})$ and $\frac{1}{\Delta y} (\widehat{N}_{k+\frac{1}{2}} - \widehat{N}_{k-\frac{1}{2}})$ respectively, where $\widehat{M}_{j+\frac{1}{2}}$ and $\widehat{N}_{k+\frac{1}{2}}$ are the numerical fluxes at the cell interface $x_{j+\frac{1}{2}}$ and $y_{k+\frac{1}{2}}$. To achieve fifth-order accuracy, the fluxes are reconstructed using the stencil of 5-cells:

$\{M_{j-2}, M_{j-1}, M_j, M_{j+1}, M_{j+2}\}$ on the x -direction and $\{N_{k-2}, N_{k-1}, N_k, N_{k+1}, N_{k+2}\}$ on the y -direction. The WENO scheme combines three candidate third-order sub-stencils into a single high-order sub-stencil using smoothness indicators and nonlinear weights. To calculate the sub-stencils, we used

WENO steps: For a fixed y_j , we considered the following stencils:

$$(24) \quad \begin{aligned} \text{Stencil 0: } & \{x_{j-2}, x_{j-1}, x_j\} \\ \text{Stencil 1: } & \{x_{j-1}, x_j, x_{j+1}\} \\ \text{Stencil 2: } & \{x_j, x_{j+1}, x_{j+2}\} \end{aligned}$$

For a fixed x_i , we also considered the following stencils:

$$(25) \quad \begin{aligned} \text{Stencil 0: } & \{y_{k-2}, y_{k-1}, y_k\} \\ \text{Stencil 1: } & \{y_{k-1}, y_k, y_{k+1}\} \\ \text{Stencil 2: } & \{y_k, y_{k+1}, y_{k+2}\} \end{aligned}$$

Again, we proceed to compute the smoothness indicator β_m as described in [17, 18] defined by:

$$(26) \quad \beta_m = \sum_{l=0}^2 \int_{x_{j-\frac{1}{2}}}^{x_{j+\frac{1}{2}}} \left(\Delta x^{l-1} \frac{d^l}{dx^l} p_m(x) \right)^2$$

where $p_m(x)$ is the polynomial on stencil m . Equation (26) must be repeated for $p_n(y)$ on stencil n . Then the reconstructed value at a point $(x_{i+1/2}, y_{j+1/2})$ is given by the weighted sum of the

polynomial reconstructions in each direction [see Appendix A]:

$$(27) \quad P(x_{i+1/2}, y_{j+1/2}) = \sum_{m=0}^2 \sum_{n=0}^2 \omega_m^x \omega_n^y p_m^x(x_{j+1/2}, y_k) p_n^y(x_j, y_{k+1/2})$$

where:

- ω_m^x and ω_n^y are the nonlinear WENO weights in the x - and y -directions, respectively.
- $p_m^x(x_{i+1/2}, y_j)$ is the polynomial reconstructed in the x -direction evaluated at $x_{i+1/2}$.
- $p_n^y(x_i, y_{j+1/2})$ is the polynomial reconstructed in the y -direction evaluated at $y_{j+1/2}$.

$$(28) \quad \omega_l = \frac{\alpha_l}{\sum_{r=0}^2 \alpha_r}, \text{ where } \alpha_l = \frac{d_l}{(\epsilon + \beta_l)^p}$$

Where $l = (m, n)$ in x - or y -direction, d_l are linear weights, β_l are smoothness indicators, ϵ is a small parameter to avoid division by zero, and $p = 2$ determines the sharpness of the transition between smooth and non-smooth regions.

For the final approximation, we combine the two spatially discretized form of the PDE to update the solution U by:

$$(29) \quad \frac{\partial U_{j,k}}{\partial t} = L(U_{j,k}) = -\frac{\widehat{M}_{j+\frac{1}{2}} - \widehat{M}_{j-\frac{1}{2}}}{\Delta x} - \frac{\widehat{N}_{j+\frac{1}{2}} - \widehat{N}_{j-\frac{1}{2}}}{\Delta y} + Q(U_{j,k})$$

Temporal Discretization. Here, the fourth-order Runge-Kutta scheme was used for the time discretization [19, 20]. The RK4 method approximates the solution $U_{j,k}(t)$ at each time step. Given the solution $U_{j,k}^n$ at time t^n , the solution $U_{j,k}^{n+1}$ at time $t^{n+1} = t^n + \Delta t$, is computed as follows:

$$(30) \quad \begin{aligned} K_1 &= L(U_{j,k}^n) \\ K_2 &= L_{j,k} \left[U_{j,k}^n + \frac{\Delta}{2} K_1 \right] \\ K_3 &= L_{j,k} \left[U_{j,k}^n + \frac{\Delta}{2} K_2 \right] \\ K_4 &= L_{j,k} \left[U_{j,k}^n + \Delta K_3 \right] \end{aligned}$$

To update $U_{j,k}$ to the next time step U^{n+1} , we use:

$$(31) \quad U_{j,k}^{n+1} = U_{j,k}^n + \frac{\Delta t}{6} (K_1 + 2K_2 + 2K_3 + K_4)$$

The RK4 integration method provides fourth-order accuracy in time, aligning well with the fifth-order spatial accuracy achieved through the WENO scheme. Time-stepping continues until $t = 1$, using a time increment of $\Delta t = 0.001$ and a spatial grid defined by $\mathcal{N}_x, \mathcal{N}_y$.

5. OPTIMAL CONTROL MODEL

To develop an optimal control model for the given COVID-19 dynamics, we incorporate control functions representing interventions such as vaccination and treatment. These controls aim to minimize both the number of infected individuals and the costs associated with implementing them over time and across the spatial domain. We define:

- $u_1(t, X)$: Control function for vaccination at location X to reduce the number of susceptible individuals who gets infected.
- $u_2(t, X)$: Control function for treatment to increase the recovery rate of infected individuals at location X .

Introducing these controls, the optimized form of system (3) becomes:

$$(32) \quad \begin{aligned} \frac{\partial S(t, X)}{\partial t} + \nabla \cdot (Sq_s) &= \Lambda - \beta S(t, X)I(t, X) - \mu S(t, X) - u_1 S(t, X) \\ \frac{\partial I(t, X)}{\partial t} + \nabla \cdot (Iq_i) &= \beta S(t, X)I(t, X) - (\gamma + \varphi + \mu)I(t, X) - u_2 I(t, X) \end{aligned}$$

Each control function $u_j(t, X)$ is estimated to lie within the range $0 \leq u_j(t) \leq 1$, with:

- $u_j = 0$: indicating no control was applied, and
- $u_j = 1$: indicating maximum effort in control.

We have that the basic reproduction number R_c of the control model (32) is:

$$(33) \quad R_c = \frac{\beta \Lambda}{(u_1 + \mu)(\gamma + \varphi + \mu + u_2)}$$

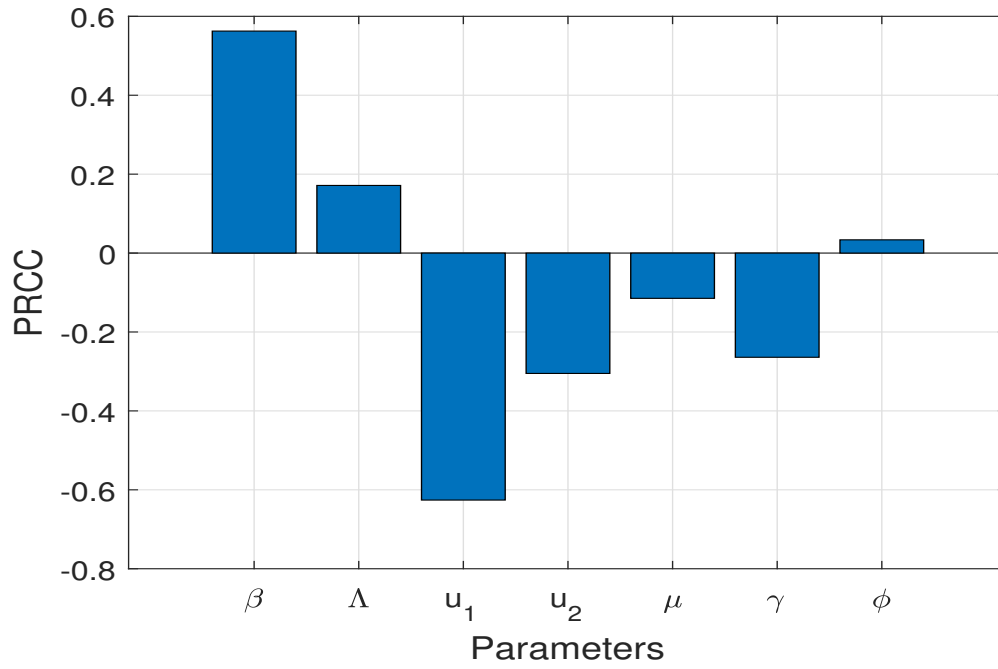


FIGURE 1. PRCC chart showing how sensitive the optimal control system (32) is to changes in its parameters.

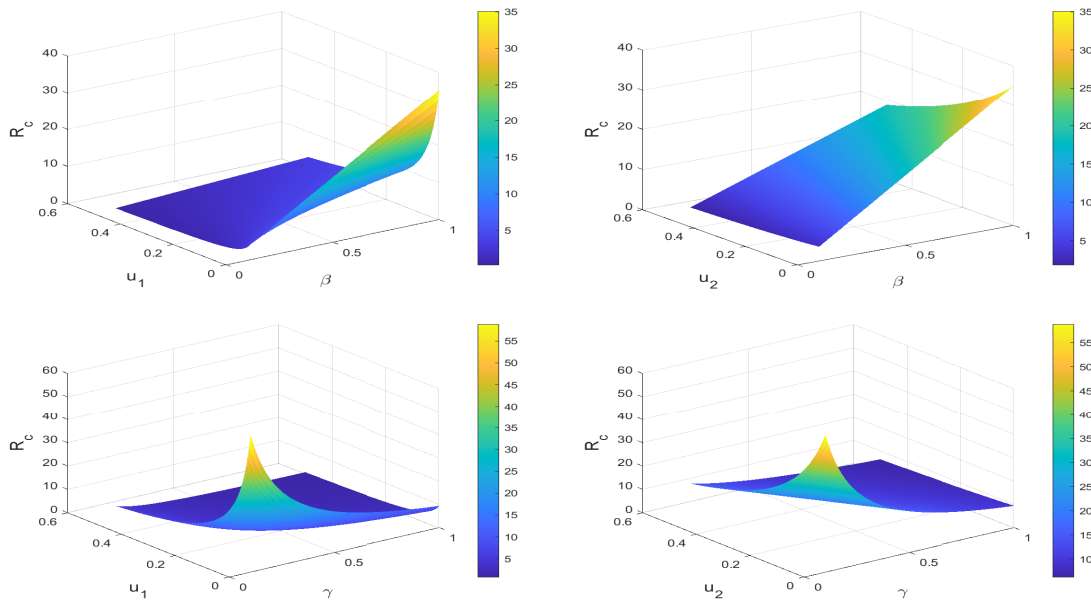


FIGURE 2. 3D contour plots illustrating the influence of some key parameters on the control reproduction number R_C .

The figure 1 above shows that a higher transmission rate (β) significantly increases the epidemic size, while immigration through birth (if not properly handled) may contribute to wider COVID-19 spread, but its influence is weaker than β . On the other hand, the control measures (u_1, u_2) has shown to be effective, with u_1 having the strongest effect in controlling the COVID outcome. Therefore, it suggests that more attention should be focused on vaccination and sensitizing individuals on the need to be vaccinated. On the other hand, Figure 2 suggests that controlling transmission (e.g., through non-pharmaceutical interventions like masking or distancing) is critical for controlling COVID-19 spread. Hence, control parameter (u_1) is highly effective, but its effect is most pronounced when combined with reductions in the contact rate β . The control parameter u_2 requires a strategic implementation to effectively reduce the COVID spread, when β is high.

We construct an objective function to minimize the spread of COVID-19. Mathematically, the minimization problem is given by the objective function:

$$(34) \quad \mathcal{J}(u_1, u_2) = \int_0^{t_f} \int_{\Omega_1} [C_1 I(t, X) + C_2 u_1^2(t, X) + C_3 u_2^2(t, X)] dX dt$$

Where $\Omega_1 \subseteq \Omega$ is a prioritized region, the constants C_1, C_2, C_3 represents the weights reflecting the relative importance of minimizing the infected population and the costs of controls, while t_f represents the final time. To address the potential nonlinear effects introduced by the controls, we use quadratic functions to evaluate cost control effectively [21, 22, 23]. For readers interested in the existence of a spatial optimal control problem, additional details can be found in the relevant literature [24, 25, 26].

The goal of the spatial model is to find the optimal control (u_1^*, u_2^*) , such that

$$(35) \quad \mathcal{J}(u_1^*, u_2^*) = \min_{u_1, u_2 \in \Omega_1} \mathcal{J}(u_1, u_2)$$

The control set of our problem is constrained as:

$$(36) \quad \Gamma = \{(u_1, u_2) \mid 0 \leq u_1(t, X) \leq u_{1,\max}, 0 \leq u_2(t, X) \leq u_{2,\max}, \forall t \in [0, t_f], X \in \Omega_1 \subseteq \Omega\}$$

Where $u_{1,\max}$ and $u_{2,\max}$ are the maximum possible levels of vaccination and treatment, determined by resource limitations. To improve the robustness and stability of the optimization

algorithm, and to keep the controls physically realistic to prevent sudden changes over time or across space, we apply smoothness constraints:

$$(37a) \quad \left| \frac{\partial u_1}{\partial t} \right| \leq \epsilon_1, \quad \left| \frac{\partial u_2}{\partial t} \right| \leq \epsilon_2$$

and

$$(37b) \quad \|\nabla u_1\| \leq \kappa_1, \quad \|\nabla u_2\| \leq \kappa_2$$

Where κ_1 and κ_2 are maximum allowable gradients for spatial smoothness, while for the temporal smoothness constraint, ϵ_1 and ϵ_2 limits the rate of change over time.

5.1. Theoretical Analysis of the Optimal Control. Pontryagin's Maximum Principle (PMP) is applied to identify the necessary conditions an optimal control must satisfy. Using this approach, equations (32) and (34) are transformed into a task of minimizing the point-wise Hamiltonian (H) with respect to the control pair (u_1, u_2) . We express the Lagrangian and Hamiltonian as:

$$(38) \quad \mathcal{L} = \int_0^{t_f} \int_{\Omega_1} \left[C_1 I + C_2 u_1^2 + C_3 u_2^2 + \lambda_S \left(\Lambda - \beta S I - \mu S - u_1 S - \nabla \cdot (S q_s) - \frac{\partial S}{\partial t} \right) \right. \\ \left. + \lambda_I \left(\beta S I - (\gamma + \varphi + \mu) - u_2 I - \nabla \cdot (I q_i) - \frac{\partial I}{\partial t} \right) + \lambda_R \left(\gamma I + u_1 S + u_2 I - \mu R - \frac{\partial R}{\partial t} \right) \right] dX dt$$

The Hamiltonian (H) is the integrand of the Lagrangian, excluding the spatial and temporal integrals. For this problem, we have:

$$(39) \quad H = C_1 I + C_2 u_1^2 + C_3 u_2^2 \\ + \lambda_S (\Lambda - \beta S I - \mu S - u_1 S - \nabla \cdot (S q_s)) \\ + \lambda_I (\beta S I - (\gamma + \varphi + \mu) - u_2 I - \nabla \cdot (I q_i)) \\ + \lambda_R (\gamma I + u_1 S + u_2 I - \mu R)$$

Where λ_S , λ_I and λ_R are the adjoint (Lagrange multiplier) variables associated with $S(t, X)$, $I(t, X)$ and $R(t, X)$ respectively.

Given an optimal control (u_1^*, u_2^*) and solutions S^*, I^*, R^* of the control system (32) that minimizes $\mathcal{J}(u_1, u_2)$ over a certain prioritize region Ω_1 , there exists adjoint variables $(\lambda_S, \lambda_I, \lambda_R)$ satisfying

$$(40) \quad \frac{\partial \lambda_S}{\partial t} + \nabla \cdot (q_s \lambda_S) = -\frac{\partial H}{\partial S}, \quad \frac{\partial \lambda_I}{\partial t} + \nabla \cdot (q_i \lambda_I) = -\frac{\partial H}{\partial I}, \quad \frac{\partial \lambda_R}{\partial t} = -\frac{\partial H}{\partial R}$$

Where

$$(41a) \quad \frac{\partial H}{\partial S} = \lambda_S(-\beta I - \mu - u_1) + \lambda_I \beta I + u_1 \lambda_R$$

$$(41b) \quad \frac{\partial H}{\partial I} = C_1 + \lambda_S(-\beta S) + \lambda_I(\beta S - (\gamma + \varphi + \mu) - u_2) + \lambda_R(\gamma + u_2)$$

$$(41c) \quad \frac{\partial H}{\partial R} = -\mu \lambda_R$$

together with no-flux boundary conditions (5) $q_s \cdot n \lambda_S = 0$, $q_i \cdot n \lambda_I = 0$, $\nabla \lambda_R \cdot n = 0$ on $\partial\Omega_1$, and the transversality conditions $\lambda_S(t_f, X) = 0$, $\lambda_I(t_f, X) = 0$, $\lambda_R(t_f, X) = 0$. Where n is the outward unit normal vector on the boundary $\partial\Omega_1$.

The optimal controls u_1^* and u_2^* minimizes H by taking the partial derivative of H with respect to u_1 and u_2 , and must satisfy the optimal condition

$$(42) \quad \frac{\partial H}{\partial u_1} = 0, \quad \frac{\partial H}{\partial u_2} = 0.$$

We therefore have

$$(43a) \quad \frac{\partial H}{\partial u_1} = 2u_1 C_2 - \lambda_S S + \lambda_R S$$

$$(43b) \quad \frac{\partial H}{\partial u_2} = 2u_2 C_3 - \lambda_I I + \lambda_R I$$

Observing condition (42), we have that the optimal control now becomes

$$(44) \quad \begin{aligned} u_1^* &= \min \left\{ 1, \max \left(0, \frac{\lambda_S S - \lambda_R S}{2C_2} \right) \right\} \\ u_2^* &= \min \left\{ 1, \max \left(0, \frac{\lambda_I I - \lambda_R I}{2C_3} \right) \right\} \end{aligned}$$

The findings show that an optimal control (u_1^*, u_2^*) exists, effectively reducing the spread of COVID-19 while implementing a dual control intervention strategy at the minimum cost.

5.2. Numerical Analysis of the Optimal Control. The numerical method outlined below offers an optimal strategy to manage the spatial spread of COVID-19, carefully balancing epidemiological needs with economic impacts. The necessary and sufficient condition for applying a numerical scheme to the optimal control model is that: (i) the system of state equation (3) must be solved forward in time, (ii) the adjoint equations must be solved backward in time, using the transversality conditions at $t = t_f$, (iii) the optimal controls $u_1^*(t, X)$ and $u_2^*(t, X)$ are updated iteratively until the solution converges to minimize the cost functional (34).

Hence, we use the finite difference method (FDM) to discretize both the time variable t , and space variable $X = (x, y)$. To proceed, we let Δt be the time step, and $\Delta x, \Delta y$ be the spatial steps for the domain $\Omega_1 \in \mathbb{R}^2$. We also define the grid: $t = n\Delta t$ for $n = 0, 1, \dots, \mathcal{N}_t$, with the uniform grid point $(\mathcal{N}_x, \mathcal{N}_y)$ of the spatial domain $x_j = j\Delta x$, and $y_k = k\Delta y$ for $j = 0, 1, \dots, \mathcal{N}_x$ and $k = 0, 1, \dots, \mathcal{N}_y$ respectively. Let $S_{j,k}^n, I_{j,k}^n$, and $R_{j,k}^n$ be the values of the state variables at grid point (j, k) and at time step n .

We note henceforth that $S_{j,k}^n \approx S(t_n, x_j, y_k)$, $I_{j,k}^n \approx I(t_n, x_j, y_k)$ and $R_{j,k}^n \approx R(t_n, x_j, y_k)$, while $\beta SI \approx \beta S_{j,k} I_{j,k}$ and so on. For the temporal derivative, we use (a forward difference) Euler discretization:

$$(45) \quad \frac{\partial S}{\partial t} \approx \frac{S_{j,k}^{n+1} - S_{j,k}^n}{\Delta t}$$

Where $\frac{\partial I}{\partial t}$ and $\frac{\partial R}{\partial t}$ follows from (45). For the spatial derivatives, we employ the central difference approximation:

$$(46) \quad \frac{\partial S}{\partial x} \approx \frac{S_{j+1,k}^n - S_{j-1,k}^n}{2\Delta x} \quad \text{and} \quad \frac{\partial S}{\partial y} \approx \frac{S_{j,k+1}^n - S_{j,k-1}^n}{2\Delta y}$$

in x - and y -directions respectively. Equation (46) is further replicated for $I(t, X)$ and $R(t, X)$. The flux terms $\nabla \cdot (Sq_s)$ and $\nabla \cdot (Iq_i)$ are handled using an upwind scheme:

$$(47) \quad \nabla \cdot (Sq_s) \approx \frac{u_{s_{j+1,k}} S_{j+1,k}^n - u_{s_{j-1,k}} S_{j-1,k}^n}{\Delta x} + \frac{v_{s_{j,k+1}} S_{j,k+1}^n - v_{s_{j,k-1}} S_{j,k-1}^n}{\Delta y}$$

Where $q_s = (u_s, v_s)$ are evaluated at cell faces. In the same manner, $\nabla \cdot (Iq_i)$ can also be formed from (47) above.

Combining the temporal (45) and spatial (47) discretization, the state equation is expressed as:

$$(48) \quad \begin{aligned} S_{j,k}^{n+1} &= S_{j,k}^n + \Delta t \left[\Lambda - \beta S_{j,k}^n I_{j,k}^n - \mu S_{j,k}^n - (u_1 S)_{j,k}^n - \nabla \cdot (S q_s)_{j,k}^n \right] \\ I_{j,k}^{n+1} &= I_{j,k}^n + \Delta t \left[\beta S_{j,k}^n I_{j,k}^n - (\gamma + \varphi + \mu) I_{j,k}^n - (u_2 I)_{j,k}^n - \nabla \cdot (I q_i)_{j,k}^n \right] \\ R_{j,k}^{n+1} &= R_{j,k}^n + \Delta t \left[\gamma I_{j,k}^n + (u_1 S)_{j,k}^n + (u_2 I)_{j,k}^n - \mu R_{j,k}^n \right] \end{aligned}$$

Next, we proceed to discretize the adjoint equations backward in time, using the backward time-stepping. From equation (40), the temporal and spatial discretization are:

$$(49) \quad \frac{\partial \lambda_S}{\partial t} \approx \frac{\lambda_S^n - \lambda_S^{n+1}}{\Delta t}$$

and

$$(50) \quad \nabla \cdot (q_s \lambda_S) \approx \frac{u_{s_{j+\frac{1}{2},k}} \lambda_S^{n+1}(j+1, k) - u_{s_{j-\frac{1}{2},k}} \lambda_S^{n+1}(j, k)}{\Delta x} + \frac{u_{s_{j,k+\frac{1}{2}}} \lambda_S^{n+1}(j, k+1) - u_{s_{j,k-\frac{1}{2}}} \lambda_S^{n+1}(j, k)}{\Delta y}$$

From equations (49) and (50), we have that the complete discretization of the adjoint equation (41a)-(41c) satisfying the transversality condition becomes:

$$(51) \quad \begin{aligned} \lambda_S^n &= \lambda_S^{n+1} + \Delta t \left[-\nabla \cdot (q_s \lambda_S^{n+1}) + \lambda_S^{n+1} (\beta I_{j,k}^{n+1} + \mu + u_1^{n+1}) - \lambda_I^{n+1} \beta I_{j,k}^{n+1} - \lambda_R^{n+1} u_1^{n+1} \right] \\ \lambda_I^n &= \lambda_I^{n+1} + \Delta t \left[-\nabla \cdot (q_i \lambda_I^{n+1}) - C_1 + \lambda_S^{n+1} \beta S_{j,k}^{n+1} - \lambda_I^{n+1} (\beta S_{j,k}^{n+1} - (\gamma + \varphi + \mu) - u_2^{n+1}) - \lambda_R^{n+1} (\gamma + u_2^{n+1}) \right] \\ \lambda_R^n &= \lambda_R^{n+1} + \Delta t \left[-\mu \lambda_R^{n+1} \right] \end{aligned}$$

Lastly, after completing the processes outlined in equations (48) and (51), the optimal controls are updated and projected onto the feasible set:

$$(52) \quad \begin{aligned} u_1^{n+1} &= \min \left\{ 1, \max \left(0, \frac{\lambda_S^{n+1} S_{j,k}^{n+1} - \lambda_R^{n+1} S_{j,k}^{n+1}}{2C_2} \right) \right\} \\ u_2^{n+1} &= \min \left\{ 1, \max \left(0, \frac{\lambda_I^{n+1} I_{j,k}^{n+1} - \lambda_R^{n+1} I_{j,k}^{n+1}}{2C_3} \right) \right\} \end{aligned}$$

The steps (45)- (52) above are repeated until the controls u_1 and u_2 converges, using the stopping criterion

$$(53) \quad \|u_1^{j+1} - u_1^j\| < \epsilon, \quad \|u_2^{j+1} - u_2^j\| < \epsilon$$

Where u_1^j, u_2^j controls u_1 and u_2 at j^{th} iteration, and u_1^{j+1}, u_2^{j+1} controls u_1 and u_2 at $j^{th}+1$ iteration (i.e. the most recent update). The norm is applied to quantify the difference between control values across the domain, while ϵ is the convergence tolerance (10^{-6}). However, convergence is reached when the u_1 and u_2 updates are smaller than ϵ for all grid points.

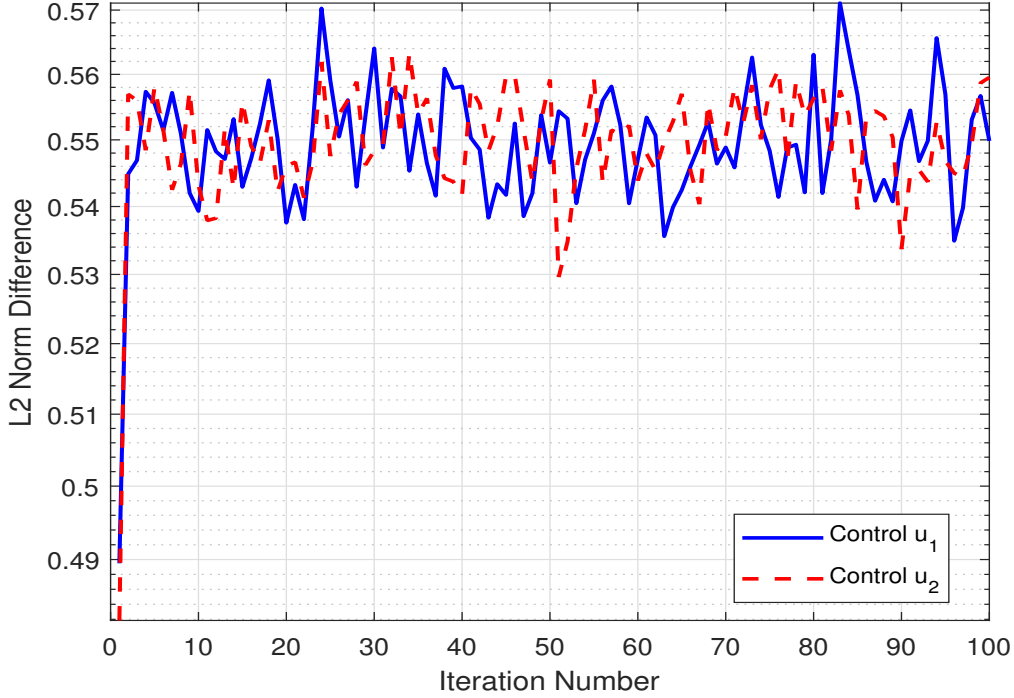


FIGURE 3. The L^2 - norm of the difference between successive controls.

Figure 3 displays the norm difference at lower cost $C_2 = C_3 = 1$. In this scenario, the controls u_1 and u_2 are less penalized, as they are easy to implement at lower cost. However, it was observed that at higher cost, it is more difficult to implement a control, and as a result, the penalty for using any of the controls (u_1, u_2) becomes more significant. The L^2 -norm difference of the controls defined by: $\|u_1^{k+1} - u_1^k\| = \sqrt{\sum_{j,k} (u_1^{k+1}(j, k) - u_1^k(j, k))^2}$ and $\|u_2^{k+1} - u_2^k\| = \sqrt{\sum_{j,k} (u_2^{k+1}(j, k) - u_2^k(j, k))^2}$, measures the difference between iterations in the controls.

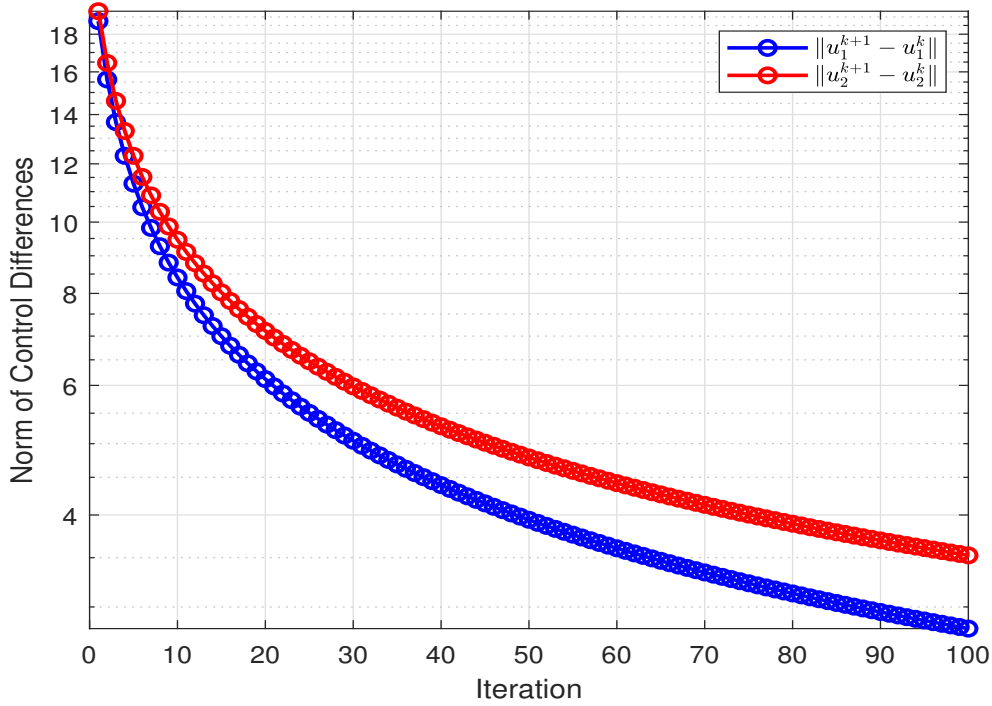


FIGURE 4. Convergence behavior of the control variables u_1 and u_2 at time step ($N_t = 100$), with a uniform grid ($N_x \times N_y$) = (100×100).

Figure 4 displays the behavior of the control convergence as iteration proceeds. First, the norms for u_1 and u_2 show monotonic convergence, which means that the optimization technique successfully stabilizes both controls. When compared to treatment options that interact with the dynamics of infection and recovery, the norm of u_1 is seen to converge more quickly, which refers to cost minimization of applying the control u_1 to the susceptible population rather than waiting till the infection explodes, to apply the control u_2 on the infected population. Consequently, u_1 can be optimized faster to mitigate the disease from spreading.

According to the convergence behavior, the control (u_2) needs more sophisticated, adaptable tactics (such as: increasing healthcare resources or enhancing treatments) in order to stabilize. On the other hand, optimizing this control necessitates more significant adjustments in order to achieve its goal of reducing the spread of COVID-19.

6. MODEL SIMULATION

The optimal control model presented above will be tested using the case of COVID-19 in Lagos State, Nigeria. Early in 2020, the COVID-19 pandemic, caused by the novel coronavirus SARS-CoV-2, became a major worldwide health emergency. On February 27, 2020, the first confirmed case was recorded in Lagos State, Nigeria. Due to its high population density, economic activity, and role as a hub for international travel, Lagos (one of Nigeria's most densely populated states and a commercial hub) became the focal point of the outbreak [27].

The population of Lagos City, a sizable metropolis in southwest Nigeria, is estimated to be 21 million, situated on an area of 1,292 *square miles* ($\approx 3,345 \text{ km}^2$) with nearly a quarter of the area dominated by water bodies that aid both local and international trade within the state and the country at large [28].

With 162,593 confirmed infection cases and 2,048 associated deaths, Nigeria was the fifth most affected country in Africa and the 77th most impacted country worldwide as of March 28, 2021. All 36 states and the Federal Capital Territory were affected by the pandemic, although Lagos State remained the epicenter, accounting for 35.4% of all cases nationally [29]. As the hardest-hit region, Lagos provides a vital case for analyzing COVID-19 dynamics and assessing the effectiveness of control measures. It also serves as a benchmark for designing interventions that can be adapted to other high-burden areas across the country [30].

Lagos State reported 27 new COVID-19 cases as of January 15, 2023, adding to Nigeria's 42 new infections during that time. This increased the total number of confirmed cases in Lagos State to 100,125 [31]. On June 25, 2022, Lagos reported a sharp increase in COVID-19 cases, with 203 new infections out of Nigeria's 247 cases recorded between June 21 and 24, 2022. By then, the total number of confirmed cases in Lagos had reached 100,125, while recording more than 754 fatalities and 79,775 confirmed cases as of December 12, 2021 [32, 33].

The cumulative plots below were further used to highlight COVID-19 cases in Lagos over a period of nine months.

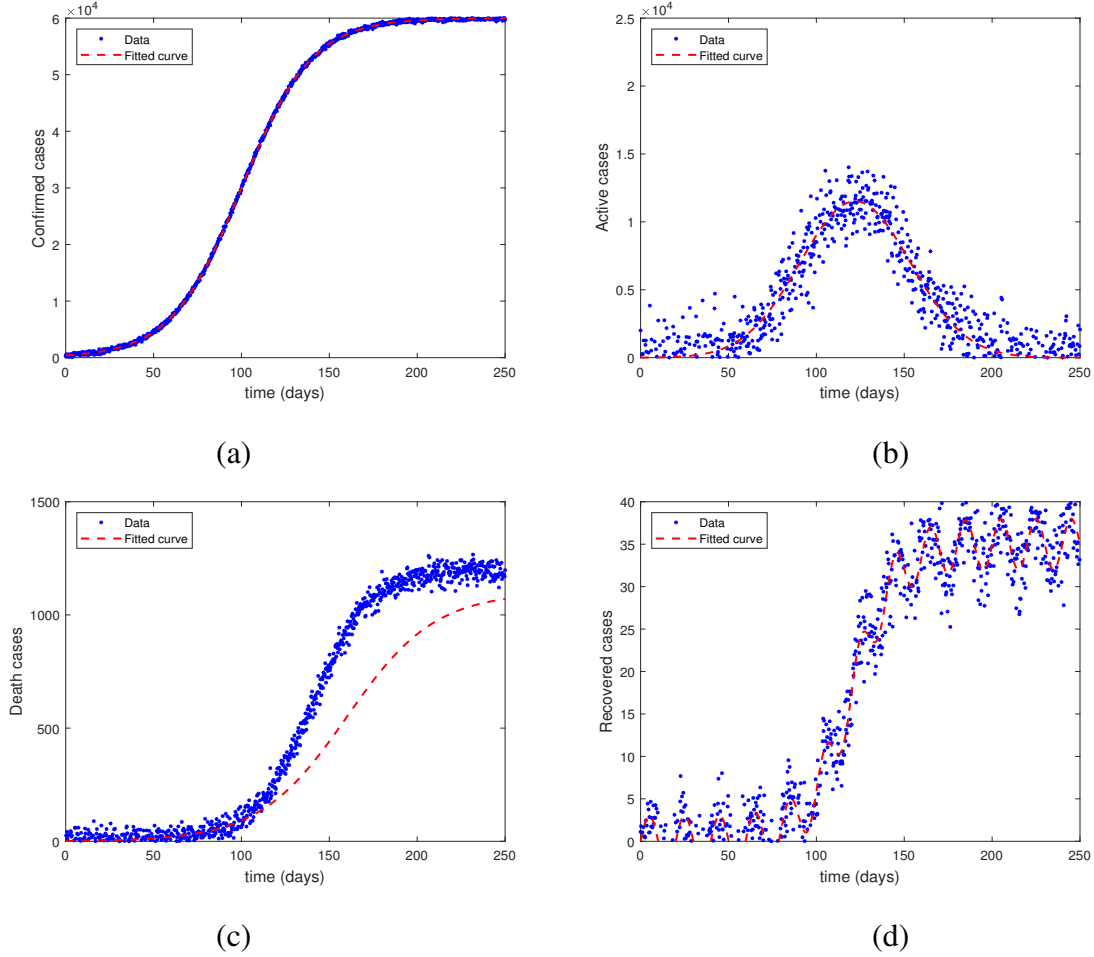


FIGURE 5. Fitted plot for the cumulative data from March 01, 2020 to November 06, 2020.

| Parameters | Range | Values | Source |
|--------------------|--------------------|-----------------------|------------|
| Λ | - | 10 | Estimated |
| β | (0,1) | 0.5426 | [34] |
| γ | (0,1) | 0.0699 | [34] |
| φ | (0,1) | 7.62×10^{-3} | [29], [35] |
| μ | (0,1) | 0.7/1,000 | [36] |
| $q_s = (u_s, v_s)$ | $0 < q_s < \infty$ | {0,1} | Fitted |
| $q_i = (u_i, v_i)$ | $0 < q_s < \infty$ | {0,1} | Fitted |

TABLE 1. Parameter values and source used for our model simulation

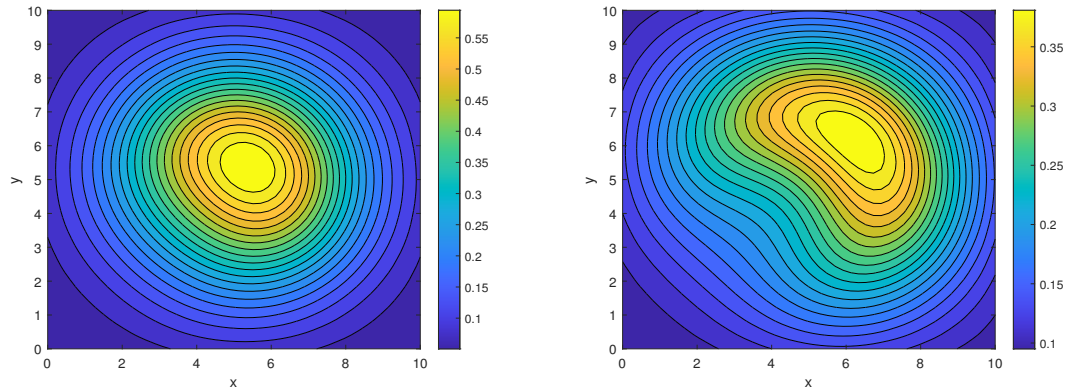
More CODID-19 data can be found at the Nigerian Center for Disease Control (NCDC) website [37], while a cumulative plot for the confirmed, active, death and recovered cases are fitted above.

The spatial domain for this research work is defined as follows:

- The set Ω represents the entire region of Nigeria.
- The subset $\Omega_1 \subseteq \Omega$ corresponds to Lagos State.

By factoring in spatial variations, our model offers valuable insights into managing and understanding the spread of COVID-19 in densely populated urban areas like Lagos, while also addressing broader transmission patterns across the country. Based on data obtained from the NCDC, the numerical simulation of our model will be presented, highlighting and discussing cases 'with control' and 'without control'.

As observed below, Figure 6 illustrates how the density of the susceptible population in Lagos State changes when COVID-19 spreads in the absence of control measures. Over time, the number of susceptible individuals decreases as more people are exposed to the virus. This pattern demonstrates that as COVID-19 spreads unchecked across the region, the pool of susceptible individuals shrinks, allowing the virus to continue spreading.



(a) Time = 5 days

(b) Time = 10 days

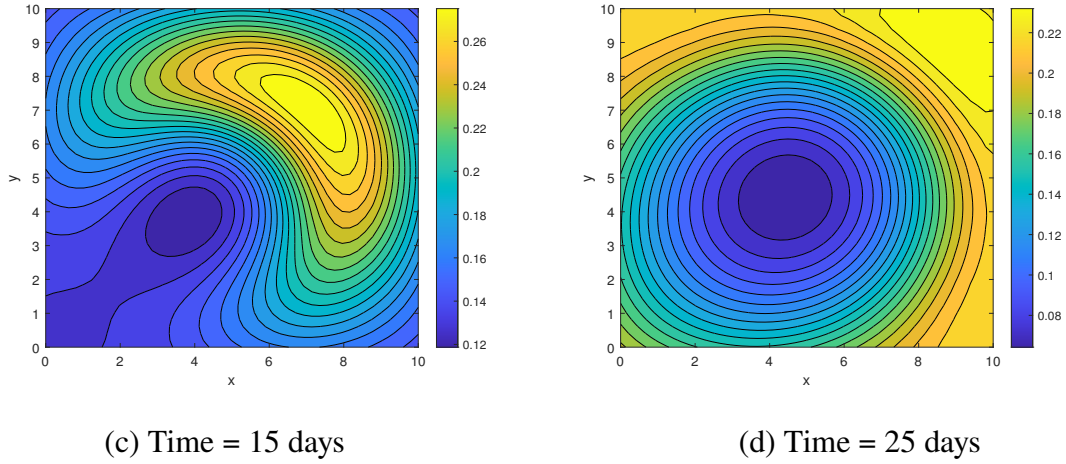


FIGURE 6. Contour plot of $S(t, x, y)$ in Lagos state, in the absence of control.

The vertical and horizontal velocity plots, are displayed below:

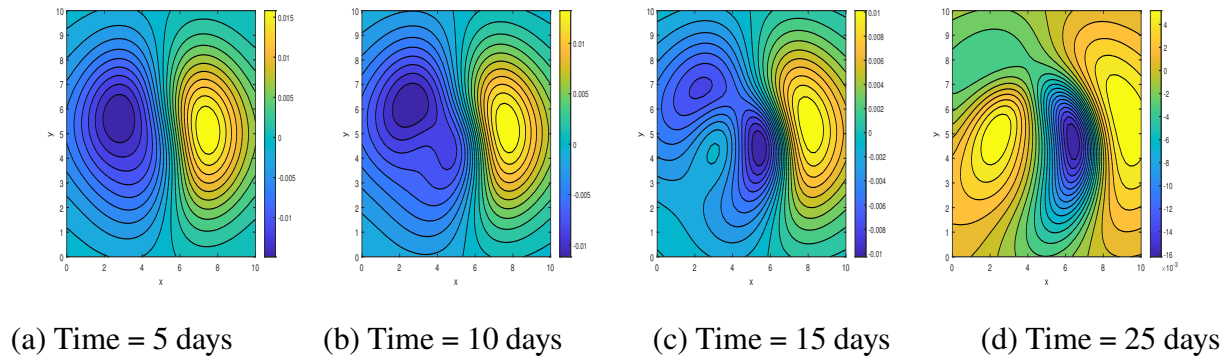


FIGURE 7. Contour plot of $u_s(t, x, y)$ for COVID-19 spread in Lagos state, with no control.

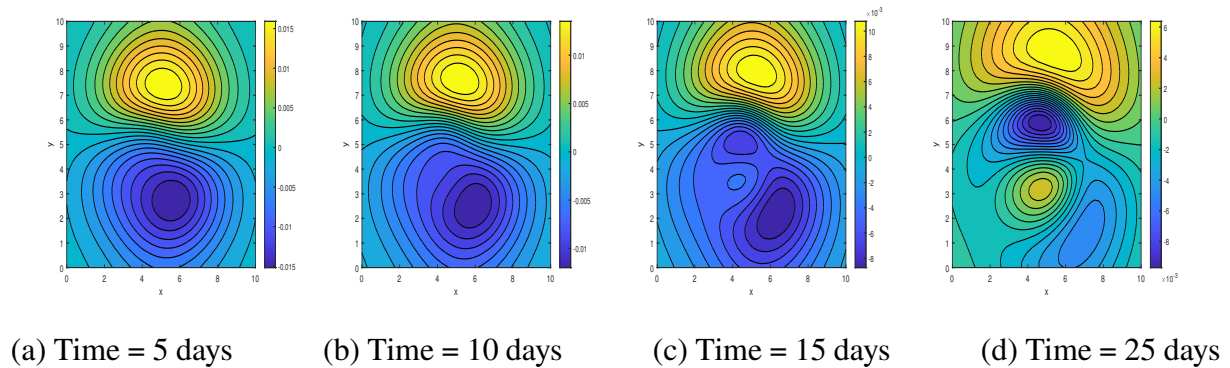


FIGURE 8. Contour plot of $v_s(t, x, y)$ for COVID-19 spread in Lagos state, with no control.

Figure 7 and Figure 8 has shown the spatial (horizontal and vertical) dynamics of the velocity profile pattern of COVID-19 spread. A close observation has revealed that the spread propagates more in the vertical direction (v_s) than in the horizontal direction (u_s) as time progresses. This suggests that the control u_1 on the susceptible population density, be applied more in the direction of higher velocity spread.

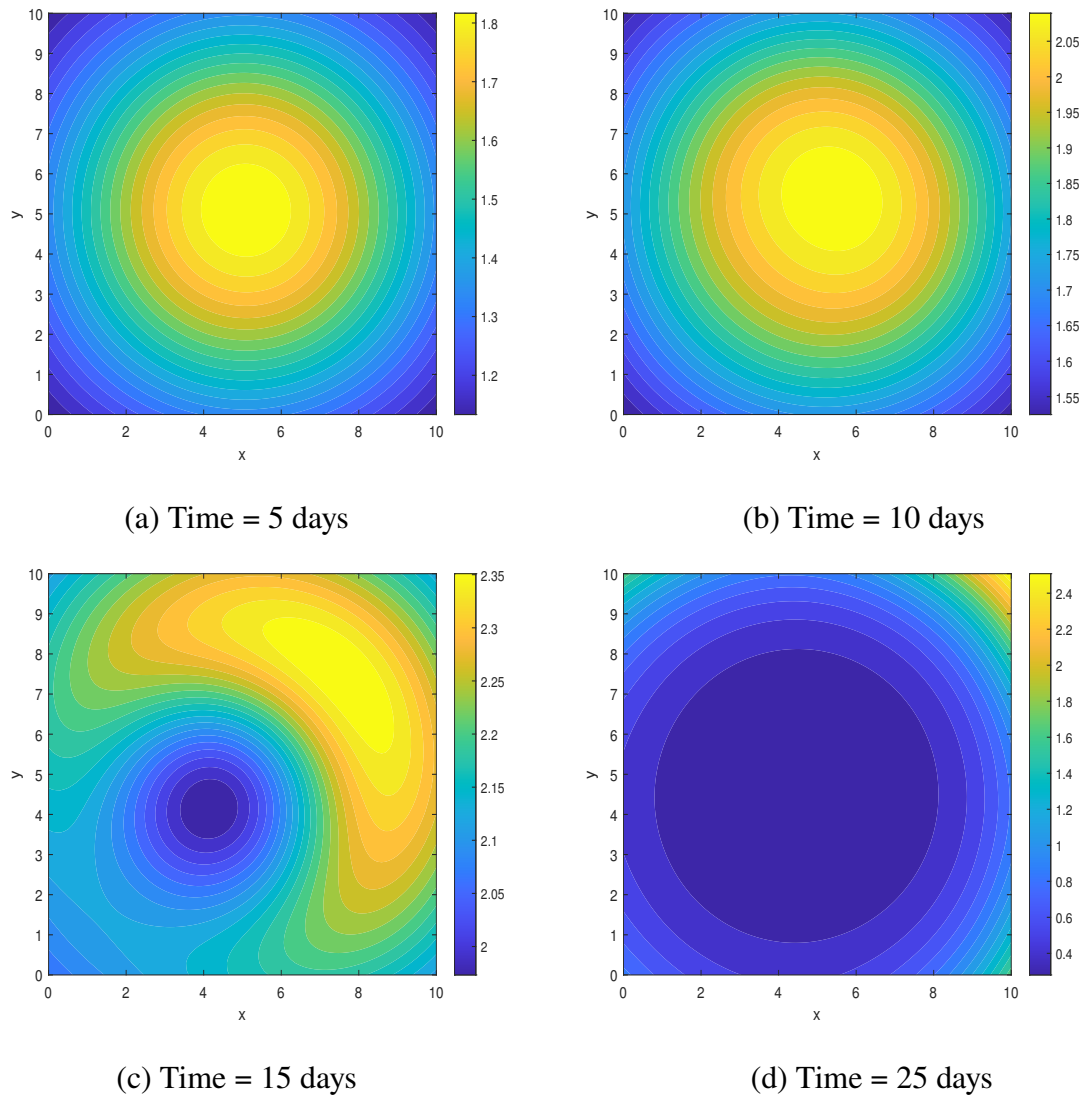


FIGURE 9. Contour plot of $S(t, x, y)$ with control in Lagos state.

A look at Figure 9 shows an improved development in the susceptible population density, when the vaccination control is applied. It is good to note that the control u_1 plays much more role in reducing the number of susceptible individuals who might be exposed to COVID-19 infection. When compared to Figure 6, the susceptible population in Figure 9 began to increase as time progresses, which implies a successful implementation of the control on susceptible population.

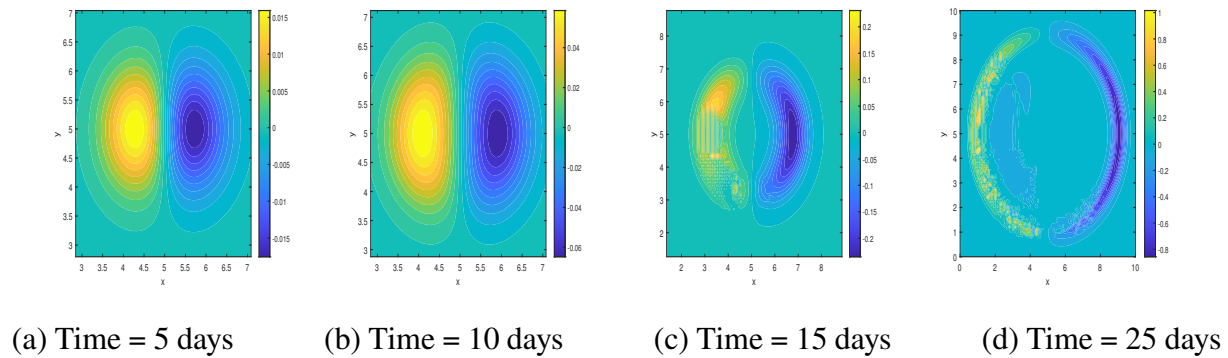


FIGURE 10. Contour plot of $u_s(t, x, y)$ with control for COVID-19 spread in Lagos state.

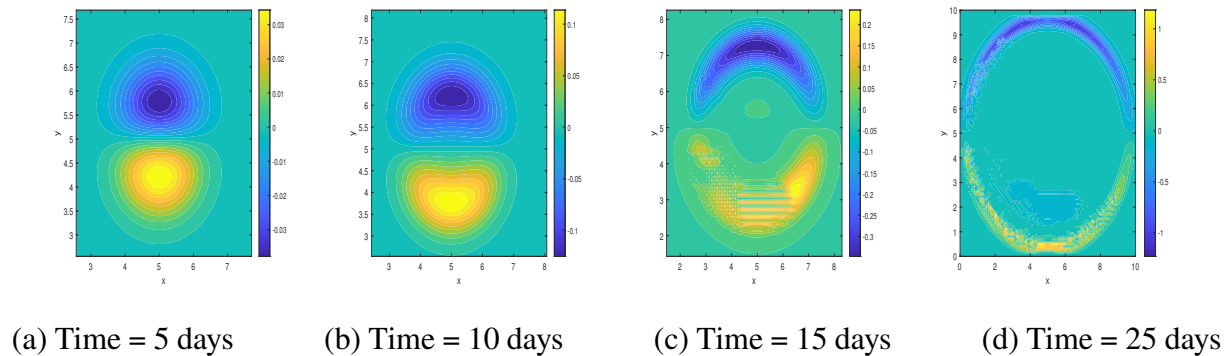
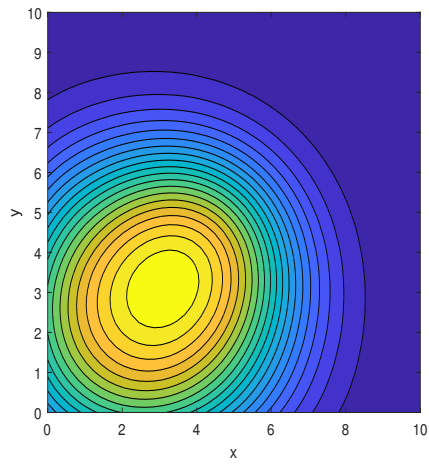
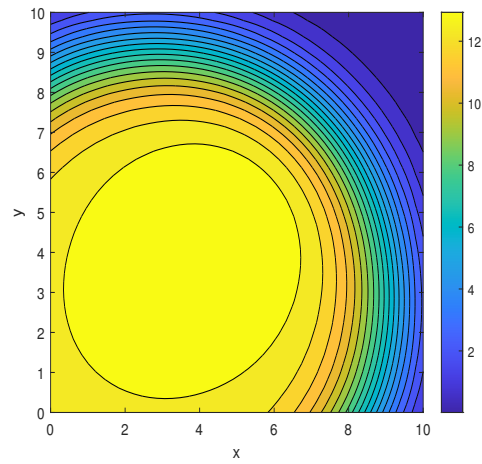


FIGURE 11. Contour plot of $v_s(t, x, y)$ with control for COVID-19 spread in Lagos state.

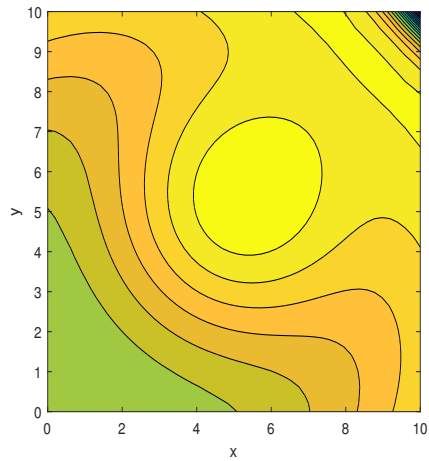
From Figure 10 and Figure 11, the velocity of spread for COVID-19 with control (u_1) was measured in the susceptible class. It was deduced that there is an improvement in recovering more susceptible individuals, and as a result, we recorded an increased velocity as compared to Figure 7 and 8 respectively.



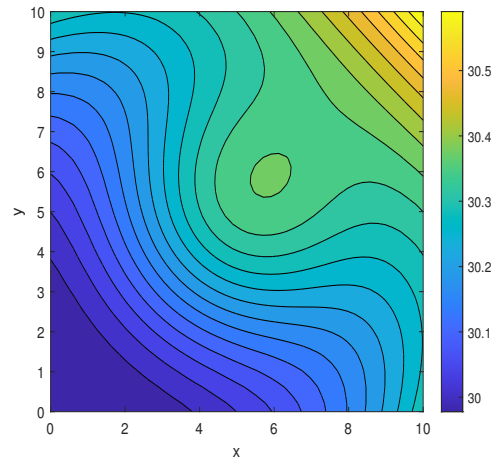
(a) Time = 5 days



(b) Time = 10 days



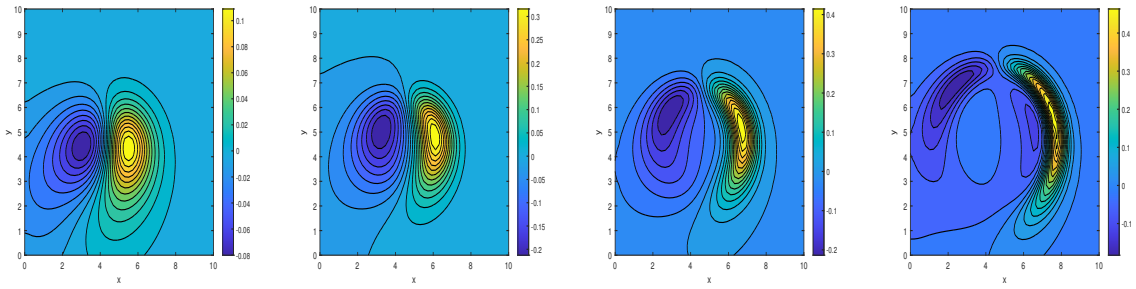
(c) Time = 15 days



(d) Time = 25 days

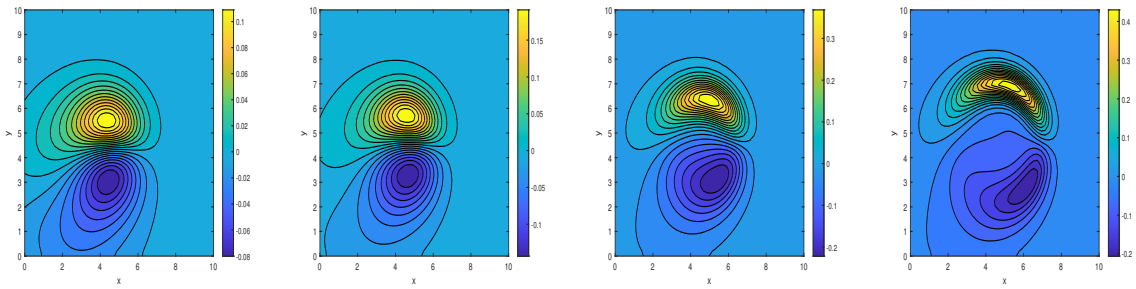
FIGURE 12. Contour plot for infected population $I(t, x, y)$ in Lagos state, in the absence of control.

The velocity profile for the infected population density with no control at different time, is displayed:



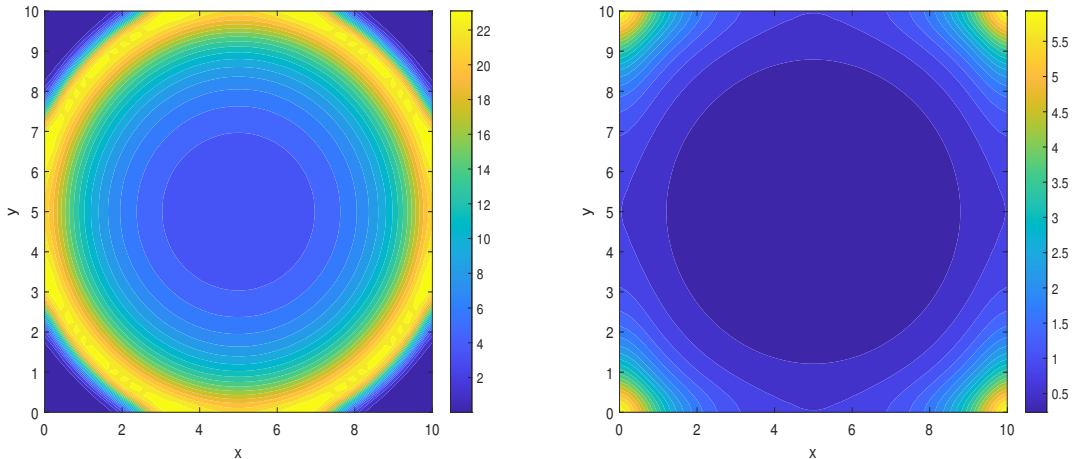
(a) Time = 5 days (b) Time = 10 days (c) Time = 15 days (d) Time = 25 days

FIGURE 13. Contour plot of $u_i(t, x, y)$ for COVID-19 spread in Lagos state, with no control.



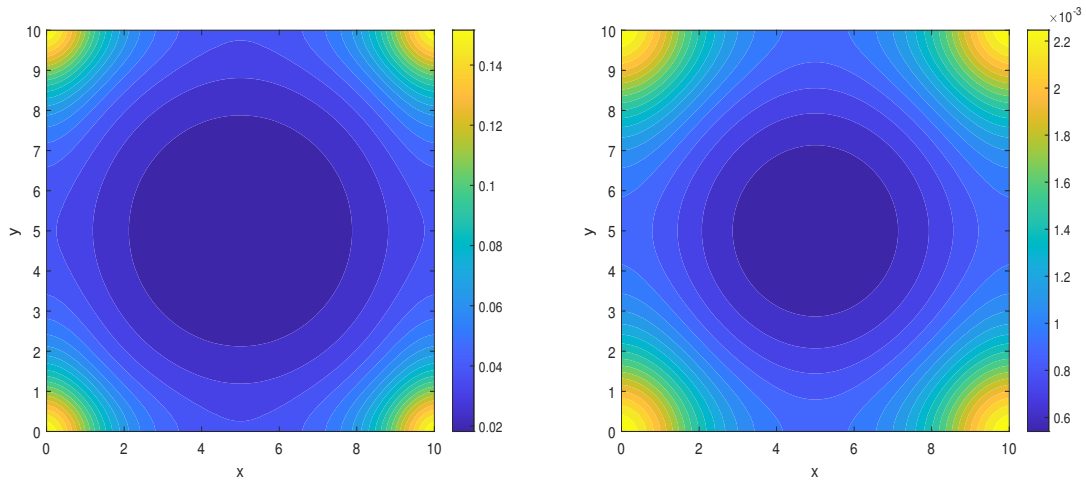
(a) Time = 5 days (b) Time = 10 days (c) Time = 15 days (d) Time = 25 days

FIGURE 14. Contour plot of $v_i(t, x, y)$ for COVID-19 spread in Lagos state, with no control.



(a) Time = 5 days

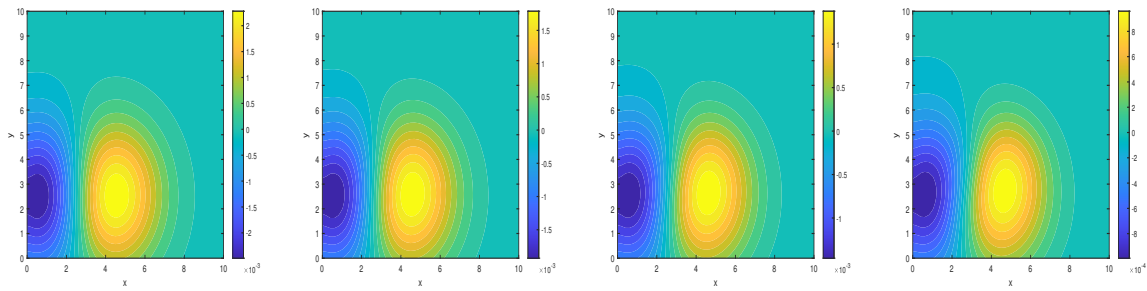
(b) Time = 10 days



(c) Time = 15 days

(d) Time = 25 days

FIGURE 15. Contour plot for the infected population $I(t, x, y)$ in Lagos state, with treatment control .



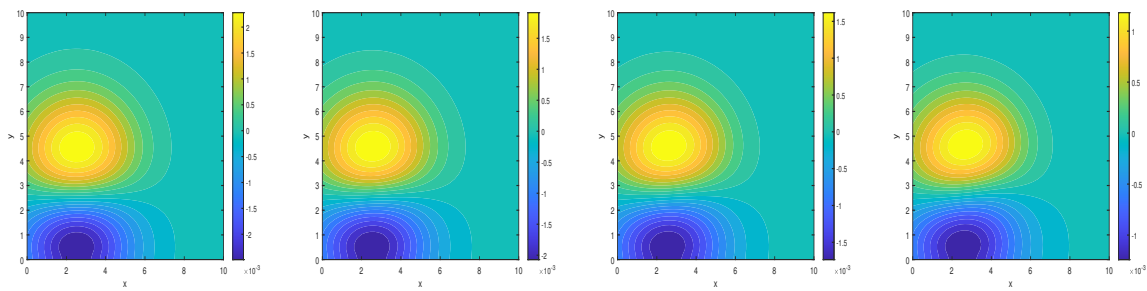
(a) Time = 5 days

(b) Time = 10 days

(c) Time = 15 days

(d) Time = 25 days

FIGURE 16. Contour plot of $u_i(t, x, y)$ with control for COVID-19 spread in Lagos state.



(a) Time = 5 days

(b) Time = 10 days

(c) Time = 15 days

(d) Time = 25 days

FIGURE 17. Contour plot of $v_i(t, x, y)$ with control for COVID-19 spread in Lagos state.

Figure 12 shows the behavior of the infected population density, at zero control. It is observed that the infected area continues to expand, showcasing the progressive spread and intensification of the infection. On the other hand, Figure 13 and Figure 14 provide insight into how quickly and in what directions the infection spreads spatially, with no control. A close observation shows that there is a rapid increase in the directional velocity $u_i(t, x, y)$, as compared to $v_i(t, x, y)$. This in essence shows the direction to which COVID-19 virus spreads more, and in such case, it is easier to know the location that needs more control.

The optimal control strategies were applied to the infected population density. Figure 15 has shown that there is some positive response to the treatment strategy (u_2) on the infected population density. Between 5-10 days, the treatment control recorded a 25% success in controlling the spread of COVID-19. The velocity profiles in Figure 16 and Figure 17 above, further opined the success of the treatment control.

6.1. General Discussion. The above graphical simulations provide a comprehensive visualization of the spatio-temporal spread of COVID-19, demonstrating the efficacy of the proposed fluid dynamics-based model. The simulations illustrate how susceptible and infected populations evolve over time, highlighting the diffusion patterns and the impact of control measures. Key observations include the transition of susceptible individuals into the infected group and the subsequent recovery process, influenced by vaccination and treatment strategies.

A significant focus is placed on the optimization parameters, which dictate the efficiency of disease control. By adjusting these parameters, such as vaccination coverage rate and treatment efficacy, the simulations reveal a marked reduction in infection peaks and an accelerated decline in active cases. The results suggest that higher vaccination rates effectively suppress the spread, while improved treatment enhances recovery, leading to a more stable system over time.

7. CONCLUSION

This study examines the interplay between susceptible and infected populations using a unique fluid dynamics analogy to propose an optimal control model for the spatial spread of COVID-19. Effectively capturing the spatiotemporal evolution of the epidemic, the model treats disease transmission as a fluid-like process governed by fluid dynamic principles. Implementing

treatment and vaccination as the main control strategies provides a flexible and dynamic approach to reducing infection spread.

Through rigorous mathematical analysis and numerical simulations, the model demonstrates its capability to optimize epidemic control strategies. The results highlight the effectiveness of early and well-calibrated interventions in reducing peak infection rates and limiting overall disease transmission. The sensitivity analyses further emphasize that even slight modifications in control parameters significantly influence the epidemic trajectory, underscoring the importance of resource allocation in public health decision-making.

This framework provides a versatile approach for modeling and controlling infectious diseases with spatial components, in addition to its direct applicability to COVID-19. By integrating concepts from epidemiology and fluid dynamics, this research offers a powerful tool for policy-makers and health authorities to develop data-driven, spatially focused intervention strategies. Future research may tend to expand this model idea to account for diverse population compositions, environmental influences, and real-world migration patterns, further enhancing its relevance for epidemic response and preparedness.

APPENDIX A. APPENDIX

Stencil Construction. The flux computation at the respective sub-stencils from Section 4 are:

In the x-direction.

$$(54) \quad \begin{aligned} \widehat{M}_{j+\frac{1}{2}}^{(1)} &= \frac{1}{3}M_{j-2} - \frac{7}{6}M_{j-1} + \frac{11}{6}M_j, \\ \widehat{M}_{j+\frac{1}{2}}^{(2)} &= -\frac{1}{6}M_{j-1} + \frac{5}{6}M_j + \frac{1}{3}M_{j+1}, \\ \widehat{M}_{j+\frac{1}{2}}^{(3)} &= \frac{1}{3}M_j + \frac{5}{6}M_{j+1} - \frac{1}{6}M_{j+2}, \end{aligned}$$

While the polynomial reconstruction for each stencils becomes:

$$\begin{aligned} p_0^x(x, y_k) &= M_{j-2} \frac{(x-x_{j-1})(x-x_j)}{(x_{j-2}-x_{j-1})(x_{j-2}-x_j)} + M_{j-1} \frac{(x-x_{j-2})(x-x_j)}{(x_{j-1}-x_{j-2})(x_{j-1}-x_j)} + M_j \frac{(x-x_{j-2})(x-x_{j-1})}{(x_j-x_{j-2})(x_j-x_{j-1})} \\ p_1^x(x, y_k) &= M_{j-1} \frac{(x-x_j)(x-x_{j+1})}{(x_{j-1}-x_j)(x_{j-1}-x_{j+1})} + M_j \frac{(x-x_{j-1})(x-x_{j+1})}{(x_j-x_{j-1})(x_j-x_{j+1})} + M_{j+1} \frac{(x-x_{j-1})(x-x_j)}{(x_{j+1}-x_{j-1})(x_{j+1}-x_j)} \\ p_2^x(x, y_k) &= M_j \frac{(x-x_{j+1})(x-x_{j+2})}{(x_j-x_{j+1})(x_j-x_{j+2})} + M_{j+1} \frac{(x-x_j)(x-x_{j+2})}{(x_{j+1}-x_j)(x_{j+1}-x_{j+2})} + M_{j+2} \frac{(x-x_j)(x-x_{j+1})}{(x_{j+2}-x_j)(x_{j+2}-x_{j+1})} \end{aligned}$$

In the y -direction.

$$(55) \quad \begin{aligned} \widehat{N}_{k+\frac{1}{2}}^{(1)} &= \frac{1}{3}N_{k-2} - \frac{7}{6}N_{k-1} + \frac{11}{6}N_k, \\ \widehat{N}_{k+\frac{1}{2}}^{(2)} &= -\frac{1}{6}N_{k-1} + \frac{5}{6}N_k + \frac{1}{3}N_{k+1}, \\ \widehat{N}_{k+\frac{1}{2}}^{(3)} &= \frac{1}{3}N_k + \frac{5}{6}N_{k+1} - \frac{1}{6}N_{k+2}, \end{aligned}$$

The polynomial reconstruction for each stencils becomes:

$$\begin{aligned} p_0^y(x_j, y) &= N_{k-2} \frac{(y - y_{k-1})(y - y_k)}{(y_{k-2} - y_{k-1})(y_{k-2} - y_k)} + N_{k-1} \frac{(y - y_{k-2})(y - y_k)}{(y_{k-1} - y_{k-2})(y_{k-1} - y_k)} + N_k \frac{(y - y_{k-2})(y - y_{k-1})}{(y_k - y_{k-2})(y_k - y_{k-1})} \\ p_1^y(x_j, y) &= N_{k-1} \frac{(y - y_k)(y - y_{k+1})}{(y_{k-1} - y_k)(y_{k-1} - y_{k+1})} + N_k \frac{(y - y_{k-1})(y - y_{k+1})}{(y_k - y_{k-1})(y_k - y_{k+1})} + N_{k+1} \frac{(y - y_{k-1})(y - y_k)}{(y_{k+1} - y_{k-1})(y_{k+1} - y_k)} \\ p_2^y(x_j, y) &= N_k \frac{(y - y_{k+1})(y - y_{k+2})}{(y_k - y_{k+1})(y_k - y_{k+2})} + N_{k+1} \frac{(y - y_k)(y - y_{k+2})}{(y_{k+1} - y_k)(y_{k+1} - y_{k+2})} + N_{k+2} \frac{(y - y_k)(y - y_{k+1})}{(y_{k+2} - y_k)(y_{k+2} - y_{k+1})} \end{aligned}$$

Smoothness Indicators. The smoothness indicators are numerically computed by:

$$(56) \quad \begin{aligned} \beta_0^x &= \frac{13}{12}(M_{j-2} - 2M_{j-1} + M_j)^2 + \frac{1}{4}(M_{j-2} - 4M_{j-1} + 3M_j)^2 \\ \beta_1^x &= \frac{13}{12}(M_{j-1} - 2M_j + F_{j+1})^2 + \frac{1}{4}(F_{j-1} - F_{j+1})^2 \\ \beta_2^x &= \frac{13}{12}(M_j - 2M_{j+1} + M_{j+2})^2 + \frac{1}{4}(3M_j - 4M_{j+1} + M_{j+2})^2 \end{aligned}$$

Similarly, for the y -direction, the smoothness indicators β_j^y are:

$$(57) \quad \begin{aligned} \beta_0^y &= \frac{13}{12}(N_{k-2} - 2N_{k-1} + N_k)^2 + \frac{1}{4}(N_{k-2} - 4N_{k-1} + 3N_k)^2 \\ \beta_1^y &= \frac{13}{12}(N_{k-1} - 2N_k + N_{k+1})^2 + \frac{1}{4}(N_{k-1} - N_{k+1})^2 \\ \beta_2^y &= \frac{13}{12}(N_k - 2N_{k+1} + N_{k+2})^2 + \frac{1}{4}(3N_k - 4N_{k+1} + N_{k+2})^2 \end{aligned}$$

CONFLICT OF INTERESTS

The authors declare that there is no conflict of interests.

REFERENCES

- [1] H. Kumar Mohajan, Mathematical Analysis of SIR Model for COVID-19 Transmission, *J. Innov. Med. Res.* 1 (2022), 1–18. <https://doi.org/10.56397/JIMR/2022.09.01>.
- [2] Y.C. Chen, P.E. Lu, C.S. Chang, T.H. Liu, A Time-Dependent SIR Model for COVID-19 With Undetectable Infected Persons, *IEEE Trans. Netw. Sci. Eng.* 7 (2020), 3279–3294. <https://doi.org/10.1109/TNSE.2020.3024723>.
- [3] I. Cooper, A. Mondal, C.G. Antonopoulos, A SIR Model Assumption for the Spread of COVID-19 in Different Communities, *Chaos Solitons Fractals* 139 (2020), 110057. <https://doi.org/10.1016/j.chaos.2020.110057>.
- [4] E. Bayraktar, A. Cohen, A. Nellis, A Macroeconomic SIR Model for COVID-19, *Mathematics* 9 (2021), 1901. <https://doi.org/10.3390/math9161901>.
- [5] X.L. Peng, Z.Q. Zhang, J. Yang, Z. Jin, An SIS Epidemic Model with Vaccination in a Dynamical Contact Network of Mobile Individuals with Heterogeneous Spatial Constraints, *Commun. Nonlinear Sci. Numer. Simul.* 73 (2019), 52–73. <https://doi.org/10.1016/j.cnsns.2019.02.004>.
- [6] Y. Tong, Z. Lin, Spatial Diffusion and Periodic Evolving of Domain in an SIS Epidemic Model, *Nonlinear Anal.: Real World Appl.* 61 (2021), 103343. <https://doi.org/10.1016/j.nonrwa.2021.103343>.
- [7] B.P. Sarangi, S.N. Raw, Dynamics of a Spatially Explicit Eco-Epidemic Model with Double Allee Effect, *Math. Comput. Simul.* 206 (2023), 241–263. <https://doi.org/10.1016/j.matcom.2022.11.004>.
- [8] Z. Cheng, J. Wang, A Two-Phase Fluid Model for Epidemic Flow, *Infect. Dis. Model.* 8 (2023), 920–938. <https://doi.org/10.1016/j.idm.2023.07.001>.
- [9] Q. Zhuang, J. Wang, A Spatial Epidemic Model with a Moving Boundary, *Infect. Dis. Model.* 6 (2021), 1046–1060. <https://doi.org/10.1016/j.idm.2021.08.005>.
- [10] D.U. Nnaji, P.R. Kiogora, I.S. Onah, J. Mung'atu, N.S. Aguegbah, Application of Fluid Dynamics in Modeling the Spatial Spread of Infectious Diseases with Low Mortality Rate: A Study Using MUSCL Scheme, *Comput. Math. Biophys.* 12 (2024), 20240016. <https://doi.org/10.1515/cmb-2024-0016>.
- [11] Z. Cheng, J. Wang, Modeling Epidemic Flow With Fluid Dynamics, *Math. Biosci. Eng.* 19 (2022), 8334–8360. <https://doi.org/10.3934/mbe.2022388>.
- [12] D.U. Nnaji, P.R. Kiogora, J. Mung'atu, N.S. Aguegbah, Spatio-Temporal Analysis of Cholera Spread: A Mathematical Approach Using Fluid Dynamics, *Model. Earth Syst. Environ.* 10 (2024), 6731–6759. <https://doi.org/10.1007/s40808-024-02151-8>.
- [13] S. Rathan, G.N. Raju, A Modified Fifth-Order Weno Scheme for Hyperbolic Conservation Laws, *Comput. Math. Appl.* 75 (2018), 1531–1549. <https://doi.org/10.1016/j.camwa.2017.11.020>.
- [14] J. Zhu, J. Qiu, A New Fifth Order Finite Difference WENO Scheme for Solving Hyperbolic Conservation Laws, *J. Comput. Phys.* 318 (2016), 110–121. <https://doi.org/10.1016/j.jcp.2016.05.010>.

- [15] F. Ferraccioli, N.I. Stilianakis, V.M. Veliov, A Spatial Epidemic Model with Contact and Mobility Restrictions, *Math. Comput. Model. Dyn. Syst.* 30 (2024), 284–302. <https://doi.org/10.1080/13873954.2024.2341693>.
- [16] P. Attard, *Non-Equilibrium Thermodynamics and Statistical Mechanics: Foundations and Applications*, Oxford University Press, 2012. <https://doi.org/10.1093/acprof:oso/9780199662760.001.0001>.
- [17] S. Zhang, C.W. Shu, A New Smoothness Indicator for the Weno Schemes and Its Effect on the Convergence to Steady State Solutions, *J. Sci. Comput.* 31 (2007), 273–305. <https://doi.org/10.1007/s10915-006-9111-y>.
- [18] C. Wu, L.g Wu, H. Li, S. Zhang, Very High Order Weno Schemes Using Efficient Smoothness Indicators, *J. Comput. Phys.* 432 (2021), 110158. <https://doi.org/10.1016/j.jcp.2021.110158>.
- [19] D. Tan, Z. Chen, On a General Formula of Fourth Order Runge-Kutta Method, *J. Math. Sci. Math. Educ.* 7 (2012), 1–10.
- [20] W. Zhao, J. Huang, S.J. Ruuth, Boundary Treatment of High Order Runge-Kutta Methods for Hyperbolic Conservation Laws, *J. Comput. Phys.* 421 (2020), 109697. <https://doi.org/10.1016/j.jcp.2020.109697>.
- [21] I.S. Onah, O.C. Collins, P.-G.U. Madueme, G.C.E. Mbah, Dynamical System Analysis and Optimal Control Measures of Lassa Fever Disease Model, *Int. J. Math. Math. Sci.* 2020 (2020), 7923125. <https://doi.org/10.1155/2020/7923125>.
- [22] M.O. Adewole, A.A. Onifade, F.A. Abdullah, F. Kasali, A.I.M. Ismail, Modeling the Dynamics of COVID-19 in Nigeria, *Int. J. Appl. Comput. Math.* 7 (2021), 67. <https://doi.org/10.1007/s40819-021-01014-5>.
- [23] A.A. Khan, S. Ullah, R. Amin, Optimal Control Analysis of COVID-19 Vaccine Epidemic Model: A Case Study, *Eur. Phys. J. Plus* 137 (2022), 156. <https://doi.org/10.1140/epjp/s13360-022-02365-8>.
- [24] A. El-Alami Laaroussi, M. Rachik, M. Elhia, An Optimal Control Problem for a Spatiotemporal SIR Model, *Int. J. Dyn. Control* 6 (2016), 384–397. <https://doi.org/10.1007/s40435-016-0283-5>.
- [25] M. Karim, S.B. Rhila, H. Boutayeb, M. Rachik, COVID-19 Spatiotemporal SIR Model: Regional Optimal Control Approach, *Commun. Math. Biol. Neurosci.* 2022 (2022), 115. <https://doi.org/10.28919/cmbn/7734>.
- [26] Z. Wang, Finite Horizon Optimal Control and Invariant Measure for a Stochastic Partial Differential Equation SIV Epidemic Model, Preprint, 2023. <https://doi.org/10.21203/rs.3.rs-3341712/v1>.
- [27] Wikipedia Contributors, Lagos — Wikipedia, The Free Encyclopedia, 2021. <https://en.wikipedia.org/wiki/Lagos>.
- [28] Encyclopaedia Britannica, Lagos State, Nigeria, February 2021. <https://www.britannica.com/place/Lagos-state-Nigeria>.
- [29] H.U. Okoroiwu, C.O. Ogar, G.M.E. Nja, et al. COVID-19 in Nigeria: Account of Epidemiological Events, Response, Management, Preventions and Lessons Learned, *Germs* 11 (2021), 391–402. <https://doi.org/10.18683/germs.2021.1276>.
- [30] World Food Programme, Lagos, Nigeria: Coronavirus is the least of concerns in the ‘Venice of Africa’, June 2020. <https://www.wfp.org/stories/lagos-nigeria-coronavirus-least-concerns-venice-africa>.

- [31] Vanguard News. Lagos tops as ncdc confirms 42 fresh cases of covid-19, January 2023. Click to view.
- [32] M. Ileyemi, Lagos Top as NCDC Confirms 42 Fresh Cases of COVID-19, December 2021. <https://www.premiumtimesng.com/news/headlines/500470-covid-19-again-lagos-tops-chart-as-nigeria-records-612-new-infections-saturday.html>.
- [33] M. Ileyemi, COVID-19: Infections Spike in Lagos as Nigeria Records 247 New Cases, June 2022. <https://www.premiumtimesng.com/news/headlines/539136-covid-19-infections-spike-in-lagos-as-nigeria-records-247-new-cases.html>.
- [34] D. Okuonghae, A. Omame, Analysis of a Mathematical Model for COVID-19 Population Dynamics in Lagos, Nigeria, *Chaos Solitons Fractals* 139 (2020), 110032. <https://doi.org/10.1016/j.chaos.2020.110032>.
- [35] Wikipedia Contributors, COVID-19 Pandemic in Nigeria — Wikipedia, The Free Encyclopedia, November 2021. https://en.wikipedia.org/wiki/COVID-19_pandemic_in_Nigeria.
- [36] Statista, Death Rate in Nigeria from 2012 to 2022, November 2021. <https://www.statista.com/statistics/580345/death-rate-in-nigeria>.
- [37] Nigeria Centre for Disease Control NCDC, COVID-19 Situation Report, November 2024. <https://ncdc.gov.ng/themes/common/files/sitreps/f2fc4aa3778e444792131765e0f81c02.pdf>.